Trend Analysis of Surface Shortwave (Solar) Radiation in Continental Northwest Territories, Canada (1980–2023)

B. D. PERSAUD,[a,b] A. R. SHAHVARAN,[b,c] G. ATTIAH,[a,c] L. E. CHASMER,[d] M. C. ENGLISH,[a]
H. KHEYROLLAH POUR,[a,c] AND B. B. WOLFE[a]

[a] *Department of Geography and Environmental Studies, Wilfrid Laurier University, Waterloo, Ontario, Canada*
[b] *Ecohydrology Research Group, Department of Earth and Environmental Sciences and Water Institute, University of Waterloo, Waterloo, Ontario, Canada*
[c] *Remote Sensing of Environmental Change Research Group, Department of Geography and Environmental Studies, Wilfrid Laurier University, Waterloo, Ontario, Canada*
[d] *Department of Geography and Environment, University of Lethbridge, Lethbridge, Alberta, Canada*

(Manuscript received 14 March 2025, in final form 3 June 2025, accepted 23 June 2025)

ABSTRACT: Identifying historical trends in surface shortwave (solar) radiation (SSR) is essential for understanding the energy balance in northern high latitudes and its effects on lake ecosystems undergoing climate-induced changes, such as those in the Northwest Territories (NWT), Canada. Using Daily Surface Meteorology and Hydrology Data (Daymet) SSR—validated against CERES measurements with an R^2 of 0.95—this study quantified SSR trends from 1980 to 2023, investigated the relationship between total cloud cover (TCC) and SSR, and assessed the sensitivity of lake surface water temperature (LSWT) to SSR changes across continental NWT. The Mann–Kendall trend analysis showed contrasting SSR trends before and after 2000 across NWT ecozones. Over the 44-yr period, western zones such as the Taiga Cordillera and Taiga Plain exhibited negative SSR trends of approximately -1.4 and -0.7 W m^{-2} decade^{-1}, respectively, whereas the eastern Taiga Shield showed an increase of about $+0.6$ W m^{-2} decade^{-1} ($p \leq 0.05$ for most areas). Seasonally, summer SSR trends were mainly negative in western regions and positive in eastern regions, underscoring complex SSR dynamics in NWT. Regarding the influence of TCC on SSR, Pearson's correlation analyses using both modeled and in situ TCC observations revealed a moderate-to-high negative correlation, particularly during spring, mainly in central and western NWT, excluding areas near the high-elevation mountainous boundaries of the Taiga Cordillera and Taiga Plains ecozones. The relationship between LSWT and SSR was varied; small lakes showed a positive correlation, while medium and large lakes located in the north exhibited negative correlations. Our findings suggest that lake thermal responses to SSR could be modulated by lake size and location, offering novel insights into NWT lake energy dynamics essential for NWT communities dependent on lakes and their ecosystems.

KEYWORDS: Shortwave radiation; Cloud cover; Remote sensing; Climate records; Trends; Arctic

1. Introduction

Incident surface shortwave (solar) radiation (SSR) is energy from the sun that reaches Earth's surface, driving both Earth's energy balance and the climate system, as well as important ecological processes (Budyko 1969; Wild 2009). Several studies have shown a global decline in annual-mean SSR (3–9 W m^{-2} decade^{-1}) from the 1950s to the 1980s, followed by an increase (1–4 W m^{-2} decade^{-1}) thereafter (Wild 2009; Yuan et al. 2021). Despite the documented importance of SSR to Earth's energy balance and the existence of historical SSR trends in regions worldwide, long-term temporal changes in SSR in Arctic regions remain understudied (Cutforth and Judiesch 2007; Weston et al. 2007; Chiacchio et al. 2010; Yuan et al. 2021; AMAP 2021). Existing studies, though limited in number and recency, indicate divergent regional trends: For example, Alaska experienced increasing SSR trends from the early 1960s to mid-1970s, followed by a predominant decrease until the late 1990s (Chiacchio et al. 2010). In contrast, a reduction in SSR by 2.25% and 2.50% per decade was documented at Alert and Resolute Bay in Nunavut, respectively, between 1964 and 2003 (Weston et al. 2007).

While external factors such as seasonal changes in Earth's orbit and solar output affect the incident SSR in Earth's stratosphere, internal factors within the troposphere, such as water vapor, aerosol type and concentration, and cloud cover, also play crucial roles in SSR trends and variability at Earth's surface (Wild 2009). Variance in SSR is primarily explained by differences in diurnal temperature range, which influence cloud formation (Bristow and Campbell 1984). The relationship between cloud cover and incoming SSR is complex, with different cloud types having distinct effects. Low clouds, for instance, have higher albedo and reflect SSR, while high-altitude clouds may allow SSR into the lower atmosphere (NASA 1999). However, an increase in high-altitude clouds can trap and then reemit longwave radiation back to the lower troposphere, leading to higher air temperature (NASA 1999). These processes collectively contribute to the amplification of climate warming when there is an increase in high-altitude clouds (NASA 1999; Abe et al. 2016; Box et al. 2019).

SSR also plays a primary driving role in both the hydrological cycle (Shook and Pomeroy 2011; Wild and Liepert 2010) and lake productivity (Tian et al. 2017; van de Poll 2021;

Denotes content that is immediately available upon publication as open access.

Corresponding author: Bhaleka Persaud, pers3479@mylaurier.ca

DOI: 10.1175/JCLI-D-25-0123.1

Adams et al. 2022) in northern regions. For instance, Hinkel et al. (2012) found that SSR strongly influenced lake near-surface temperature during summer, resulting in temperature increases of 1.0°–4.0°C at two lakes near Barrow, Alaska. Schmid and Köster (2016) reported that approximately 40% of the spring and summer lake surface temperature increases at Lake Zurich, Switzerland, were attributed to increasing SSR between 1981 and 2013. In the northern latitude regions of Canada, lakes play a vital role in regional energy balance due to high heat and energy storage capacity, facilitating the exchange of heat, energy, and water and regulating evaporation, runoff, and basin water storage (Oswald and Rouse 2004; Rouse et al. 2005). SSR, longwave radiation, and latent heat fluxes predominantly contribute to the energy budget of most lakes (Fink et al. 2014; Schmid and Read 2022). However, our understanding of how lake water temperatures vary in response to changes in SSR remains limited, despite the ecological significance of lakes and their potential as indicators of climate warming (Adrian et al. 2009; O'Reilly et al. 2015; Fabris et al. 2020).

Canada's Changing Climate Report (Bush and Lemmen 2019) acknowledges the importance of SSR as a climate variable but focuses its review on air temperature, precipitation, and other lake ecosystem indicators during the past five decades without incorporating SSR trends. This is due to a scarcity of in situ SSR data, which is a result of the paucity of actinometric stations and relatively few long-term SSR measurements in high-latitude regions (Przybylak et al. 2021; Diaconescu et al. 2023). Consequently, long-term trends in global and regional climate change are determined based largely on surface air temperature, where long-term records are available typically near areas with higher population density (Arias et al. 2021). Estimates of SSR can be derived from model reanalysis data, remote sensing observations, and spatially interpolated diurnal temperature-range-based modeled data when in situ measurements of SSR are unavailable (Bristow and Campbell 1984; Hungerford et al. 1989; Thornton and Running 1999). Temperature-based SSR models assume that maximum air temperature decreases with lower atmospheric transmissivity, while minimum air temperature increases with increased cloud cover (Bristow and Campbell 1984; Hungerford et al. 1989). Conversely, clear-sky conditions result in greater maximum air temperatures due to high SSR and minimum air temperatures decrease due to reduced atmospheric emissivity (Bristow and Campbell 1984; Hungerford et al. 1989). These temperature-based SSR estimates closely align with available in situ SSR data for North America and elsewhere, offering wide spatiotemporal coverage (Bristow and Campbell 1984; Hungerford et al. 1989; Hasenauer et al. 2003; Stettz et al. 2019; Thornton et al. 2021; Yuan et al. 2021), and have been used to characterize SSR variability and trends (e.g., Wild 2009; Yuan et al. 2021). However, limited attention has been paid to quantifying long-term patterns in SSR and the implications of changing SSR patterns on northern lakes. These temperature-based models provide extensive spatiotemporal coverage and may help improve our understanding of SSR variability in northern Canada and its impact on ice-free season lake temperatures, which have implications for the timing of the freeze-up process on lakes.

As outlined in preceding paragraphs, previous studies have focused on trends in SSR and lake surface water temperature (LSWT) on a global and continental scale. However, the high degree of spatiotemporal variability in these trends (Wild 2009; Yuan et al. 2021; O'Reilly et al. 2015) warrants further investigation at the regional and local levels at northern high latitudes. Hence, the objectives of this research are 1) to quantify the spatiotemporal trends of SSR in continental Northwest Territories (NWT), Canada, from 1980 to 2023, 2) to explore whether observed changes in SSR can be attributed to cloud cover, and 3) to evaluate the relations between LSWT and SSR trends by focusing on lakes in the North Slave Region (NSR), NWT, as a case study. This research aims to advance our understanding of spatiotemporal patterns of SSR and potential implications for lake energy balance during the warm season. Detecting and understanding changes in SSR is crucial, as it significantly influences Earth's energy budget and may impact the rate at which the atmosphere and lakes warm. Warming has already impacted the rate of permafrost thaw and productivity of lakes, both of which have been documented in the NWT since the 1980s (Kwong and Gan 1994; Rouse et al. 1997; Kuhn and Butman 2021; DeBeer et al. 2021).

2. Study area

The study area, located in the continental NWT (Canada), spans seven ecozones from the Boreal Plain at 60°N to the Arctic Ocean at 70°N, from the Boreal Cordillera and Taiga Cordillera in the west to the Taiga Shield and southern Arctic in the east, covering an area of 1.0 million km^2 (Fig. 1). The region is dominated by Arctic and sub-Arctic continental climates, characterized by short cool summers and long cold winters (Phillips 1990). Although much surface water is present, this region is considered relatively dry (Phillips 1990). This can be attributed to low total annual precipitation, averaging between 200 and 400 mm per year, with at least 50% falling as snow between November and March (Phillips 1990; Bailey et al. 1997). Summer air temperatures in this region are highest in July (mean daily air temperature ranging from 7° to 17°C) and lowest in January (mean daily air temperature varies from −29° to −17°C) [Environment and Climate Change Canada (ECCC) 2022]. SSR is at a minimum in winter months due to the reduced daylight hours and the variable high solar zenith angle (Bailey et al. 1997). Consequently, the persistence of snow and ice during this period causes a significant proportion of the incoming solar radiation to be reflected back to the atmosphere due to the albedo effect (Bailey et al. 1997; Serreze and Barry 2014). In contrast, during the summer months, when Earth's Northern Hemisphere is tilted toward the sun, SSR reaches its maximum, with June experiencing the highest levels of SSR (Bailey et al. 1997).

Objective 3 of this study focuses on examining the relationship between SSR and LSWT, with particular emphasis on the North Slave Region due to its high density of lakes (approximately 38% of NWT lakes are located in the North Slave Region; Messager et al. 2016). The North Slave Region comprises a diverse landscape of forest, grassland and shrubs, wetlands,

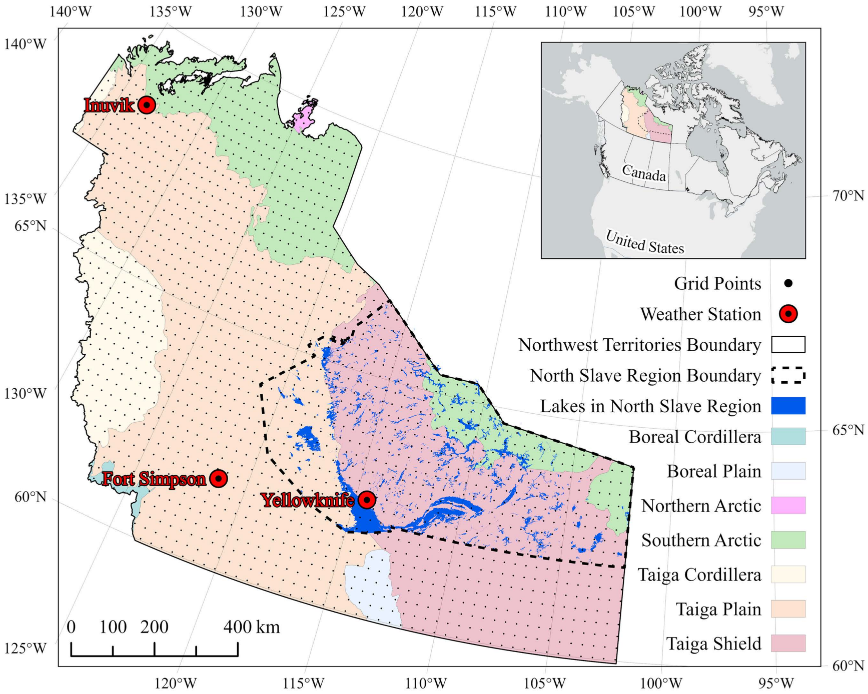

FIG. 1. The map illustrates the study area, highlighting grid points (black dots) defined at a 0.25° × 0.25° (latitudinal and longitudinal) resolution across the NWT to extract spatially consistent pairwise matchups (corresponding pixels) from datasets with varying spatial resolutions. The map also depicts the ecozones of NWT in distinct colors, with three independent weather stations marked by red and black circles (Inuvik, Fort Simpson, and Yellowknife). The NSR is outlined with a dashed black boundary, and the selected lakes within this region are represented in blue.

rivers, and lakes, with approximately 24% of the surface area covered with wetlands, rivers, and lakes (Ecosystem Classification Group 2009).

3. Data and methods

a. Datasets

Continuous and long-term in situ climate data are spatially and temporally limited in NWT due to the remoteness and expansive territory of this northern region (Mekis et al. 2018). To address this limitation, Daily Surface Meteorology and Hydrology Data (Daymet) SSR interpolated data (~1-km grid resolution) from Oak Ridge National Laboratory Distributed Active Archive (ORNL DDAA) were used. These data were employed to examine the temporal variation of SSR receipt across the study area. Additionally, fifth generation European Centre for Medium-Range Weather Forecasts (ECMWF) atmospheric reanalysis (ERA5) total cloud-cover (TCC) data (~31-km grid resolution) from the ECMWF were used to determine the correspondence between cloud cover and SSR. To assess relations between LSWT responses to SSR, Landsat-derived LSWT data (30-m resolution) were used. These datasets were used to understand changing trends in SSR for the following reasons: 1) They fill the significant gap in in situ observations by providing continuous and long-term spatiotemporal data (daily estimates of SSR and ERA5 since 1980 and 16-day overpass of LSWT data since 1984) and 2) these databases are freely distributed and easily accessible. Additional details on these datasets are provided in the following paragraphs.

1) SSR DATA

The Daymet SSR dataset provides estimates of incident shortwave radiation (srad), which represents the combined total of direct and diffuse solar radiation received at Earth's surface. This value is expressed as the average flux density over the daylight period of each day (Thornton et al. 1997; Thornton and Running 1999; Thornton et al. 2021). Daymet version 4 data, spanning 1980–2023, were utilized in this study. Thornton et al. (2021) computed incoming SSR using the Mountain Microclimate Simulation Model, version 4.3 (Bristow and Campbell 1984; Hungerford et al. 1989; Thornton and Running 1999). This model utilizes in situ daily minimum and maximum air temperature and daily precipitation from ECCC weather stations, along with other geographic attributes such as elevation, coordinates, and solar zenith angle, to generate SSR over Canada (Thornton and Running 1999; Thornton et al. 2021). In any given year, at least 1000–1500 in situ Canadian stations were used in Daymet to develop interpolated gridded products at 1-km resolution over Canada, but the quantity of in situ locations in northern Canada was much smaller when compared with southern Canada. Daymet SSR has a relatively low mean error [0.02 megajoule (MJ) m^{-2}; maximum error of 2.5 MJ m^{-2}] compared with SSR in areas with dense networks of weather stations; however, mean bias increases in areas with sparse monitoring networks, as expected (Thornton et al. 2000; Hasenauer et al. 2003; Thornton et al. 2021). Additionally, Daymet SSR was evaluated against NASA's Clouds and the Earth's Radiant Energy System (CERES) daily solar insolation data across NWT for the period 2006–23. The analysis revealed highly consistent seasonal and interannual patterns between Daymet SSR and CERES, with a correlation coefficient R^2 of 0.95 as outlined in the supplemental figures (Fig. A1a in the appendix). Additional details on Daymet modeled SSR data generation and validation can be found in Thornton et al. (1997) and Thornton et al. (2000, 2021).

In this study, daily Daymet SSR was extracted from grid points (Fig. 1) across the continental NWT. The daily data were aggregated to compute annual and seasonal average SSR for each year (1980–2023). The meteorological seasons analyzed were defined as spring (March–May), summer (June–August), autumn (September–November), and winter (December–February), temporally consistent with prior SSR trend studies (Chiacchio et al. 2010; Yuan et al. 2021).

We selected the year 2000 as a breakpoint to compare the 1980–2000 and 2001–23 trends of SSR based on multiple lines of published evidence suggesting that significant environmental transitions occurred in the NWT around this time. For example, Connon et al. (2014) identified the period from mid-1990s to early 2000s as a period of pronounced thaw-induced runoff and hydrological changes, linked to permafrost degradation. Chasmer and Hopkinson (2017) noted significant changes in the landscape and the threshold losses of discontinuous permafrost that began around this time, particularly following the 1997–98 El Niño event, which triggered accelerated thaw. Similarly, Haynes et al. (2019) described thaw-induced land-cover changes, including the rapid transformation of forested peat plateaus into wetlands at the southern margin of discontinuous permafrost in northeastern British Columbia and southwestern NWT, associated with accelerating permafrost loss and accompanied by increased runoff reported at several in situ stations around the turn of the century.

2) TCC DATA

To investigate the influence of cloud cover on modeled incoming SSR, ERA5 TCC data were used as they provide spatial coverage across NWT, coincident with Daymet modeled radiation. ERA5 is the fifth generation ECMWF atmospheric reanalysis, developed as an improvement from its predecessor ERA-Interim (Hersbach et al. 2020), which assimilates several moisture-sensitive satellite channels, thereby improving estimates of cloud-covered areas (Hersbach et al. 2020). ERA5 has a spatial resolution of approximately 31 km, and data are available from 1979 to the present at an hourly scale. In this study, ERA5 total cloud data from 1980 to 2023 were extracted for the continental NWT to address objective 2. Correlation analyses between Daymet daily SSR and ERA5 daily TCC were conducted separately for each meteorological season (as defined above) to assess seasonal variations in their relationship. Daily ERA5 TCC data were also compared with Moderate Resolution Imaging Spectroradiometer (MODIS) daily cloud fraction (CLDFR) products from both *Terra* and *Aqua* satellites during the period 2000–23 (Fig. A1b in the appendix). Derived from level-3 cloud properties products at a 1-km resolution and first collected by the *Terra* satellite in 1999, MODIS provides data on cloud-cover totals, although it covers a shorter historical period than ERA5. The time series comparison shows that both datasets effectively capture the temporal variability of cloud cover, reflected by an R^2 value of 0.26 (Fig. A2b in the appendix). Additionally, to independently evaluate the SSR–cloud-cover relationship, in situ TCC observations from three NWT stations—Fort Simpson, Yellowknife, and Inuvik (Fig. 1)—archived by ECCC for 1980–2020 were analyzed alongside the modeled ERA5 TCC–Daymet SSR data. The in situ data are based on frequent (1–3 h) human-estimated observations at meteorological stations operated by NAV Canada and represent the line of sight of TCC (Milewska 2004). To visualize the relationship between Daymet SSR and in situ cloud-cover observations on a common scale, we normalized the coinciding daily matchup pairs (corresponding pixels) at these stations (1980–2020) by converting each variable to z scores or anomaly (subtracting the mean and dividing by the standard deviation), enabling them to be plotted together.

3) LSWT DATA

Remotely sensed LSWT data were used to investigate the variability of LSWT in relation to SSR, as in situ lake water temperature observations are sparse for lakes in the NWT (Attiah et al. 2023). Remote sensing is a useful method for estimating LSWT, as demonstrated in previous studies (e.g., Wloczyk et al. 2006; Dörnhöfer and Oppelt 2016; Pareeth et al. 2016; Schaeffer et al. 2018; Sharaf et al. 2019; Vanhellemont 2020; Kheyrollah Pour et al. 2012, 2014a,b). For example, Pareeth et al. (2016) reported that differences [root-mean-square error (RMSE)] between satellite-derived thermal and measured lake surface temperature ranged from 0.38° to 1.28°C in a subalpine lake. Huang et al. (2017) found an RMSE of 0.41°C when comparing Landsat-derived and in situ lake surface temperature for five lakes in Alaska.

In this study, over 500 lakes in the North Slave Region (Fig. 1) were selected for analysis. These lakes were classified into three categories based on their surface area: small (<1 km^2), medium (1–100 km^2), and large (>100 km^2), following the classification by Rouse et al. (2005). Lake boundaries were obtained from the HydroLAKES database (Messager et al. 2016). Surface temperature data were derived from the thermal infrared (TIR) band of Landsat 5, 7, and 8 between 1984 and 2020 (referred to as North Slave Region LSWT). A detailed description of the data generation process can be found in Attiah et al. (2023). A comparison between the North Slave Region Landsat-derived LSWT and in situ surface water temperature measurements from 2014 to 2019 showed a mean bias of 0.12°C and an RMSE of 1.7°C (Attiah et al. 2023). To investigate the relationship between LSWT and SSR, the corresponding Daymet SSR values for each lake, from its centroid pixel, were extracted, and then, Pearson's correlations were computed over the summertime series.

All SSR–LSWT pairs are restricted to the core summer months (June–August) to ensure ice-free conditions. After applying the quality control steps described by Attiah et al. (2023)—cloud masking via the Landsat Quality Assessment (QA) band, a 100-m inward buffer to avoid shoreline mixing, z-score-based outlier removal, and water-ice pixel classification—we retained 245 187 daily LSWT records across over 500 lakes (see Fig. A3 for their distribution).

b. *Statistical analysis*

The statistical analyses in this study were conducted using Python version 3.8, leveraging several key libraries including *(geo)pandas* for (geo-)data handling; *numpy* for numerical operations; *rasterio, netCDF4*, and *arcpy* for spatial data processing; *scipy.stats* for statistical computations; *pymann-kendall* for trend analysis; and *matplotlib and seaborn* for visualization.

To determine the significance and rate of change, this study used the nonparametric Mann–Kendall (MK) test and the Theil–Sen slope estimator (Mann 1945; Kendall 1970; Yue et al. 2002). The MK test offers several advantages: It does not require normally distributed residuals, is less sensitive to outliers, and is widely used in climatology for detecting monotonic trends, thus enhancing the comparability of our results with existing literature (Yuan et al. 2021; Diksha et al. 2022; Wang et al. 2023). Furthermore, in addition to analyzing the overall period from 1980 to 2023, we performed separate trend analyses for the 1980–2000 and 2001–23 subperiods, which addresses uncertainties associated with potential nonlinear behavior and changing environmental conditions over time. The MK test is utilized to identify trends in time series data without assuming any specific distribution. It evaluates the null hypothesis of no trend against the alternative hypothesis of an increasing or decreasing trend. The test statistic, Kendall's tau (τ), quantifies the strength and direction of the trend, and the associated p value assesses the significance of the observed trend (pertaining to the MK test), indicating the probability that the observed trend occurred by chance under the null hypothesis. The Theil–Sen estimator calculates the median slope of all possible pairwise combinations of data points, providing a robust estimate of the trend slope that is less sensitive to outliers compared to linear regression (Mann 1945; Kendall 1970; Yue et al. 2002).

For examining the relationships between any two variables mentioned in this study, we employed Pearson's correlation coefficient (Wilks 2006). The p value associated with each correlation coefficient assesses the probability that the observed correlation occurred by random chance under the null hypothesis of no association between the variables. Here, statistical significance is defined as $p \leq 0.05$, unless otherwise stated. The choice of Pearson's correlation was motivated by the continuous and approximately Gaussian distribution of our daily SSR (Fig. A4) and cloud-cover datasets, making it more suitable for detecting linear relationships compared to nonparametric methods such as Spearman's correlation. Pearson's correlation coefficient r is defined as

$$r = \frac{\sum(X_i - \overline{X})(Y_i - \overline{Y})}{\sqrt{\sum(X_i - \overline{X})^2 \sum(Y_i - \overline{Y})^2}}, \qquad (1)$$

where X_i and Y_i are the individual sample points and $\overline{X}$ and $\overline{Y}$ are the means of the variables.

We conclude this section with Fig. 2, which provides a schematic workflow diagram summarizing the key steps undertaken in the methodology of this paper. The diagram demonstrates the datasets used, preprocessing and processing stages, and final outputs, including technical validations, spatiotemporal trends, and correlations. The region of interest (ROI) for all processed outputs is the NWT, except for two outputs focusing on three meteorological stations within NWT and all lakes in the North Slave Region; similarly, while the temporal coverage was intended to span from 1980 to 2023 to align with the primary objective, some outputs exhibit slightly shortened periods due to limitations in data availability and accessibility. This visualization highlights how different datasets and processes were systematically applied for trend analysis, spatial correlations, and technical validation, leading to the final outputs presented to address each objective.

4. Results

a. *Characterizing trends in annual- and seasonal-mean SSR in the NWT*

1) ANNUAL-MEAN SSR TRENDS

During the entire 44-yr period from 1980 to 2023, NWT displayed a heterogeneous spatiotemporal mosaic of mean annual Daymet SSR trends, with individual ecozones diverging markedly in both direction and magnitude of change. The Taiga Cordillera ecozone has the greatest long-term decline, with an overall decrease of -1.4 W m^{-2} decade^{-1}, which is approximately twice the magnitude of reductions observed in the northern Arctic, Taiga Plain, and Boreal Cordillera, each at around -0.7 W m^{-2} decade^{-1} over the same 44-yr window (Fig. 3). The Taiga Cordillera's pattern is not uniformly negative. During the earlier 1980–2000 period, the Taiga Cordillera experienced a positive mean trend of $+1.3$ W m^{-2} decade^{-1}, with spatial variability spanning a wide range (-16.3 to $+14.4$ W m^{-2} decade^{-1}; Fig. 3a), before reversing sharply to -4.3 W m^{-2} decade^{-1} after 2000 (Fig. 3b). This temporal change highlights that even within a single ecozone, SSR dynamics can undergo dramatic regime shifts. The Boreal Cordillera ecozone, by contrast, is unique for its consistently negative SSR trends throughout both time periods, starting at -3.3 W m^{-2} decade^{-1} in 1980–2000 (Fig. 3a) and reducing only slightly to -2.9 W m^{-2} decade^{-1} after 2000 (Fig. 3b), underlining persistent low SSR conditions in the southwestern NWT. Other ecozones reveal different temporal dynamics. The northern Arctic, which began with a negative trend (-0.8 W m^{-2} decade^{-1}) in the 1980–2000 era, shifted to a positive trend ($+1.1$ W m^{-2} decade^{-1}) in the 2001–23 period. Similarly, the southern Arctic transitioned from a negligible

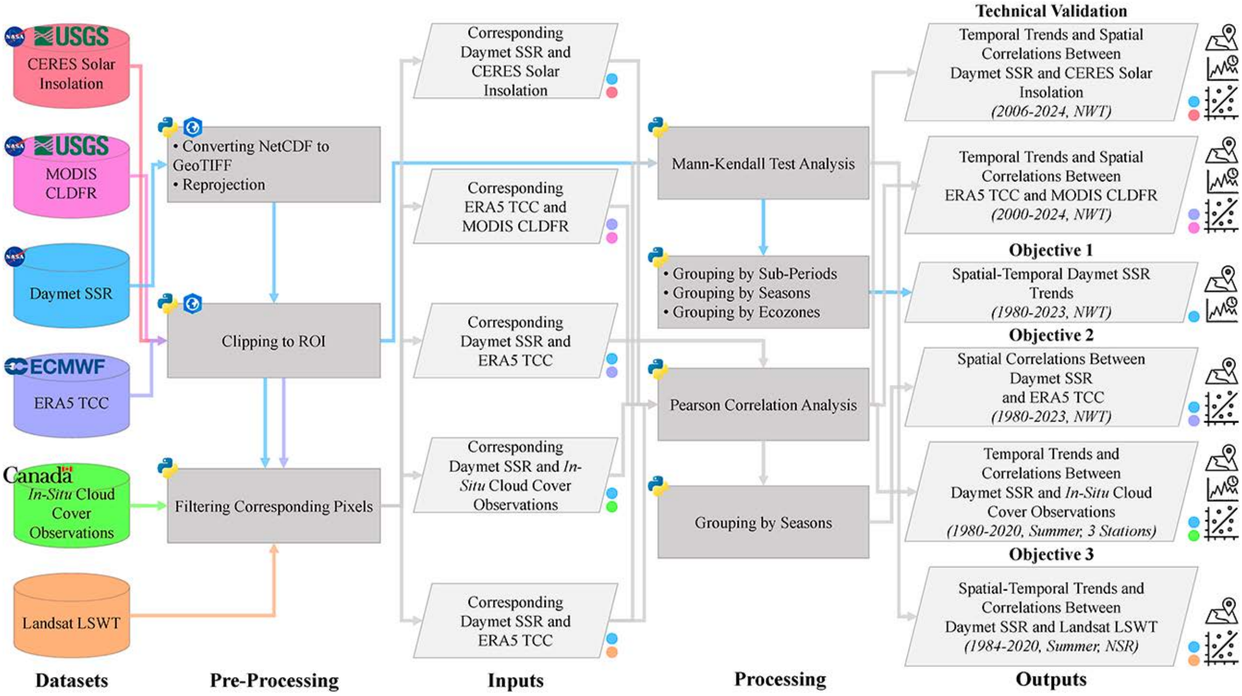

FIG. 2. Schematic workflow diagram of the methodology, illustrating the datasets utilized and preprocessing and processing steps, along with their respective inputs and outputs. The cylinders, rectangles, and trapezoids represent the datasets, inputs/outputs, and processes, respectively. Color-coded markers next to each trapezoid indicate the corresponding datasets used in each calculation step. The types of reported results—spatial analysis, trend analysis, and correlation analysis—are depicted as maps, time series, and correlation icons, respectively, next to the final outputs. Temporal coverage and the ROI for each output are provided in italicized parentheses.

negative trend (-0.2 W m^{-2} decade^{-1}) to a modest positive one ($+0.3$ W m^{-2} decade^{-1}). The Taiga Plain also reversed direction, shifting from a strongly negative trend (-2.1 W m^{-2} decade^{-1}) to a slightly positive trend ($+0.2$ W m^{-2} decade^{-1}). Notably, both the Taiga Shield and Boreal Plain (located in the southeastern part of the NWT) saw their long-term SSR trajectories trend positively over 1980–2023 (Fig. 3c), at $+0.6$ and $+0.2$ W m^{-2} decade^{-1}, respectively, with the Taiga Shield starting negative and ending positive and the Boreal Plain undergoing a substantial shift from -2.1 to $+2.0$ W m^{-2} decade^{-1} between the two intervals (Table 1).

Over the entire study period, the NWT exhibited a small negative trend of -0.3 W m^{-2} decade^{-1}. A summary of the statistics discussed here is presented in Table 1, and two supplemental figures (Fig. A4, displaying a ridgeline plot of annual-mean Daymet SSR distributions over NWT from 1980 to 2023, and Fig. A5, showing the time series plot with linear trend lines) are provided in the appendix.

2) SEASONAL-MEAN SSR TRENDS

The analysis showed distinct and diverse seasonal patterns in SSR trends that aligned with the seasons and ecozones across NWT between 1980 and 2023 (Fig. 4). During spring (Fig. 4a), incoming SSR generally increased in the eastern ecozones, with the southern Arctic and Taiga Shield exhibiting positive trends of $+0.9$ and $+1.0$ W m^{-2} decade^{-1}, respectively. In contrast, the western regions tended toward negative trends for spring, most notably in the Taiga Cordillera at -2.4 W m^{-2} decade^{-1}. A similar spatial pattern occurred in summer (Fig. 4b), where the Taiga Cordillera (-2.8 W m^{-2} decade^{-1}) and Taiga Plain (-2.6 W m^{-2} decade^{-1}) to the west showed notable declines, while parts of the Taiga Shield, in the southeast, remained positive ($+0.4$ W m^{-2} decade^{-1}). The highest slope during the warm seasons occurred in the Taiga Cordillera, with -2.4 and -2.8 W m^{-2} decade^{-1} in spring and summer, respectively. Within this ecozone, summer exhibited particularly large spatial variability, ranging from -14.2 to $+10.2$ W m^{-2} decade^{-1}. For the colder seasons, especially winter (Fig. 4d), no significant overall trends were observed during the past 44 years. Similarly, some ecozones recorded only small changes even during warmer seasons such as the Taiga Shield (spring: $+1.0$ W m^{-2} decade^{-1} and summer: $+0.4$ W m^{-2} decade^{-1}), Boreal Plain in spring (-0.2 W m^{-2} decade^{-1}), and northern Arctic in spring ($+0.4$ W m^{-2} decade^{-1}). Across the entire NWT, seasonal trends were generally negligible or weak, except in summer, where the territorial mean displayed a decline of -1.6 W m^{-2} decade^{-1}. For autumn (Fig. 4c), the northern Taiga Cordillera exhibited negative mean trends, while the southern Taiga Cordillera and southern Taiga Shield ecozones both showed positive mean trends ($+1.0$ W m^{-2} decade^{-1}). A summary of the statistics discussed here is presented in Table 2. Note that while our analysis includes all ecozones, we recognize that SSR estimates in high-elevation regions (Taiga Cordillera and Boreal Cordillera) may carry greater uncertainty due to limited in situ calibration points, complex topographic

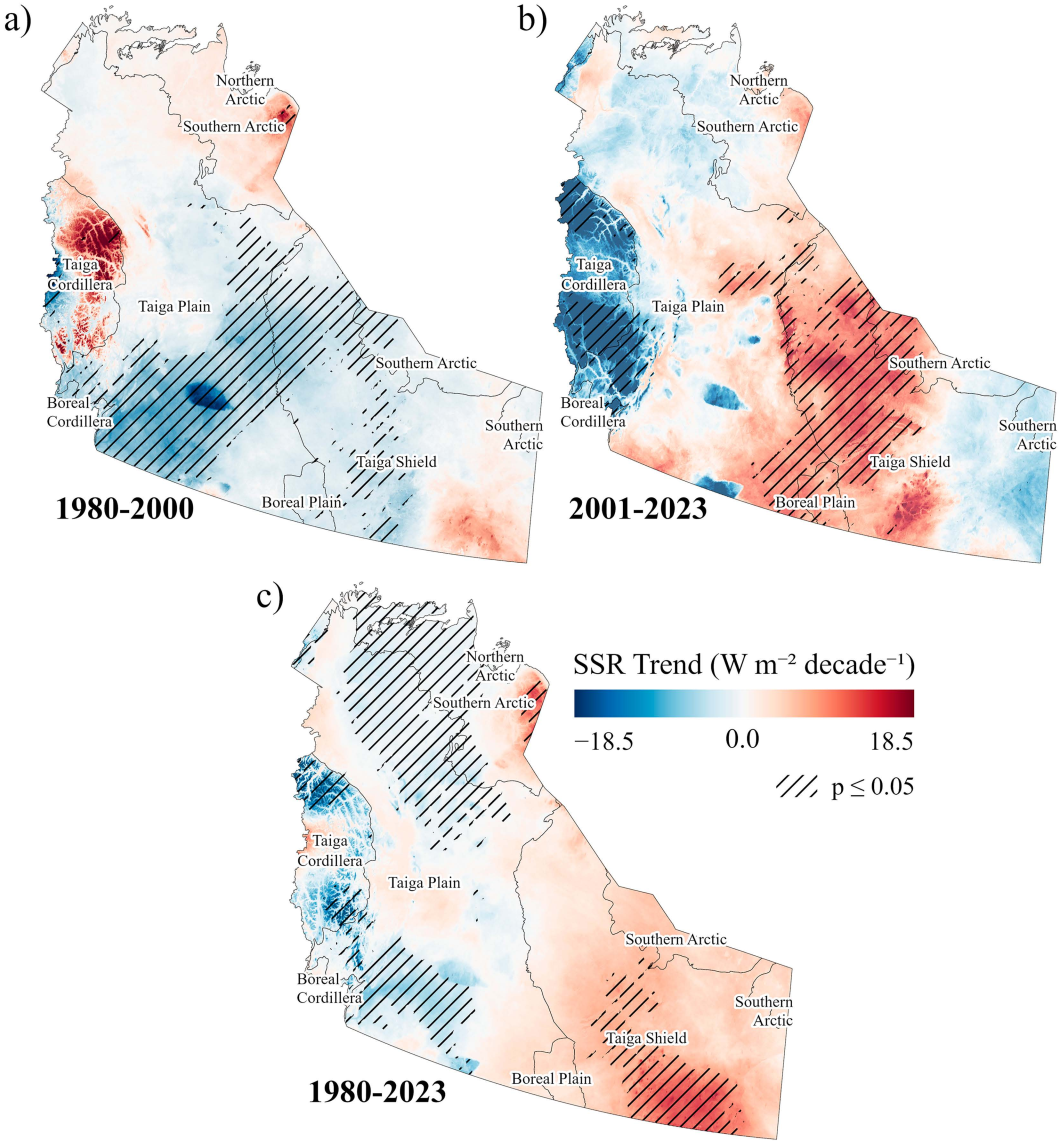

FIG. 3. Spatial distribution of SSR trends across the NWT for the periods: (a) 1980–2000, (b) 2001–23, and (c) 1980–2023. Trends were derived from mean annual Daymet SSR data (native resolution: ~1 km) using the MK test. The color bar represents the rate of change (Sen's slope), while shaded areas denote statistical significance (at $p \le 0.05$).

shading, and steeper radiative gradients. Even though the Daymet SSR data are validated against CERES daily solar insolation data across NWT, the Taiga Cordillera and Boreal Cordillera ecozones may exhibit larger model errors than lower-elevation areas. We therefore interpret these trends tentatively and recommend viewing them in the context of the broader spatial variability illustrated in Figs. 3 and 4.

b. Correlation between TCC and SSR

The analysis focused on examining the relationship between TCC and SSR to determine the extent to which TCC influences the detected SSR trends (Figs. 5 and 6) across the NWT. Initially, this relationship was examined at three locations (Inuvik, Yellowknife, and Fort Simpson) where independent measurements of in situ TCC data were available. The correlation coefficients were negative at Inuvik ($r = -0.54$, $p \le 0.05$), Yellowknife ($r = -0.57$, $p \le 0.05$), and Fort Simpson ($r = -0.24$, $p \le 0.05$) (Figs. 5 and 6), indicating that SSR decreases as cloud cover increases, as expected. Figure 5 also shows that in most years when TCC exceeded its long-term average, SSR was typically below its long-term average and vice versa. Increasing TCC and decreasing SSR variability were observed from 2001 through 2020 (ranging from ±1 standard deviation) for Inuvik and Yellowknife when compared to the remainder of the time series (Fig. 6).

Similar to the relationship between SSR and in situ TCC, the correlation coefficient between Daymet SSR and ERA5 TCC was also mostly negative, ranging from −0.45 to 0 (Fig. 7). SSR

TABLE 1. Statistics of the mean annual Daymet SSR (Sen's slope; $\mathrm{W\ m^{-2}\ decade^{-1}}$) trend magnitude across the NWT and its ecozones over the analyzed periods. These values are the averages of the pixel trends within each ecozone (NA = northern Arctic; SA = southern Arctic; TC = Taiga Cordillera; TP = Taiga Plain; TS = Taiga Shield; BC = Boreal Cordillera; BP = Boreal Plain; NWT = Northwest Territories). Values in parentheses indicate the range (minimum, maximum) of pixel slopes within each ecozone, and values in square brackets indicate the percentage of each ecozone's area where the trend is statistically significant ($p \le 0.05$).

	NA	SA	TC	TP	TS	BC	BP	NWT
Area ($\mathrm{km^2}$)	2351	175 257	83 819	511 664	343 222	5102	16 728	1 138 142
1980–2000	−0.8	−0.2	1.3	−2.1	−1.6	−3.3	−2.1	−1.4
	(−1.3, 0.0)	(−3.6, 8.3)	(−16.3, 14.4)	(−13.4, 7.4)	(−5.4, 7.3)	(−5.5, 1.6)	(−3.5, −0.9)	(−16.3, 14.4)
	[0%]	[6%]	[6%]	[32%]	[28%]	[42%]	[6%]	[25%]
2001–23	1.1	0.3	−4.3	0.2	1.2	−2.9	2.0	0.2
	(0.6, 1.5)	(−1.9, 3.6)	(−17.6, 0.7)	(−15.5, 3.8)	(−2.7, 6.1)	(−18.8, 1.2)	(0.9, 2.9)	(−18.8, 6.1)
	[0%]	[8%]	[39%]	[12%]	[34%]	[22%]	[53%]	[21%]
1980–2023	−0.7	−0.2	−1.4	−0.7	0.6	−0.7	0.2	−0.3
	(−0.8, −0.5)	(−2.0, 2.6)	(−8.6, 2.1)	(−5.7, 0.9)	(−0.9, 3.3)	(−5.0, 0.1)	(−0.2, 0.6)	(−8.6, 3.3)
	[0%]	[44%]	[25%]	[34%]	[21%]	[8%]	[0%]	[30%]

was negatively correlated with cloud cover, notably during the spring months, although the relationship was less pronounced in the rest of the seasons. Strong negative correlations were predominantly clustered over the Taiga Plains ecozone during spring, with values lower than −0.40 (Fig. 7). Except for certain areas in northern and northeastern ecozones, which showed near-zero correlation, all other ecozones exhibited negative correlations. The overall (for the entire 1980–2023 period) correlation map of ERA5 TCC and Daymet SSR corresponding pixels is presented in Fig. A6 in the appendix.

We note that our correlations between SSR and TCC use the daily average TCC from ERA5, which includes both daylight and nighttime values. Focusing only on midday or daylight-hour cloud cover could strengthen correlations in seasons with short days (autumn–spring) by more directly linking cloudiness to incoming solar radiation. We acknowledge that relying on 24-h averages may introduce some uncertainty and could slightly attenuate correlation magnitudes outside of summer; however, comparisons of SSR against both modeled TCC (Fig. 7) and in situ cloudiness (Fig. 6) yield consistent negative correlations of similar magnitude, supporting the robustness of our findings.

Furthermore, in high latitudes, outside the summer season, increased cloud cover can produce a net warming effect at the surface by enhancing downwelling longwave radiation even as it reduces incoming SSR. While our SSR–LSWT correlations focus on the ice-free summer window (June–August), when clouds primarily cool by reflecting shortwave radiation, we recommend that future work incorporate downward longwave flux from reanalysis (e.g., ERA5) to fully capture the radiative impact of clouds on lake surface temperatures in spring, autumn, and winter.

c. Correlation between SSR and LSWT in the North Slave Region

In the North Slave Region, characterized by the high density of lakes, the relationship between SSR and LSWT was explored. It was observed that approximately 14% of lake areas exhibited increasing SSR trends, with rates ranging from +0.5 to +3.6 $\mathrm{W\,m^{-2}\,decade^{-1}}$, while the remaining 86% of lakes showed decreasing SSR trends, with rates varying from −0.1 to −11.0 $\mathrm{W\,m^{-2}\,decade^{-1}}$, between 1984 and 2020 (Fig. 8a). During the same period, 45% of lakes showed a significant increasing trend of Landsat-derived LSWT, with the rate of change ranging from +1.2 to +4.6°C ($p \le 0.05$) (Fig. 8b).

The distribution of correlation coefficients indicated spatial heterogeneities between SSR and LSWT, which might coincide with the northern tree line boundary in the North Slave Region (Fig. 9a). Positive correlations were primarily found for lakes in the western part of the region, near Great Slave Lake (south of the tree line), while negative correlations were prevalent for lakes in the southern, northern, and easternmost parts of the North Slave Region (northern tree line). In fact, 91 of the 92 lakes with statistically significant positive correlations lie south of the tree line, whereas 56 of the 57 lakes with statistically significant negative correlations lie north of it. Furthermore, small lakes exhibited a stronger positive correlation between SSR and LSWT compared to medium and large lakes (Fig. 9b). With respect to lake size, 87% of small lakes ($n = 62$) exhibited a positive correlation, whereas 77% of medium lakes ($n = 464$) and 91% of large lakes ($n = 12$) predominantly showed negative correlation between SSR and LSWT (Fig. 9b). Notably, geographic location relative to the tree line and lake size do not fully overlap—several of the medium-to-large lakes with negative correlations lie south of the tree line—indicating that both spatial position and lake size must be jointly considered to understand SSR–LSWT dynamics in the North Slave Region.

5. Discussion

This study analyzed trends in SSR spanning four decades (1980–2023) across the continental NWT. Multiple data sources, including Daymet interpolated SSR data, ERA5 reanalysis TCC data, and Landsat-derived LSWT estimates, were used for analysis. Results indicate a general decrease in mean SSR between 1980 and 2000, followed by an increase in mean SSR in most ecozones between 2001 and 2023 (Fig. 3). These SSR trends, in terms of both directions and magnitudes, align with previous studies that used other datasets (including in situ data) and focused on other geographical areas in northern high latitudes during earlier

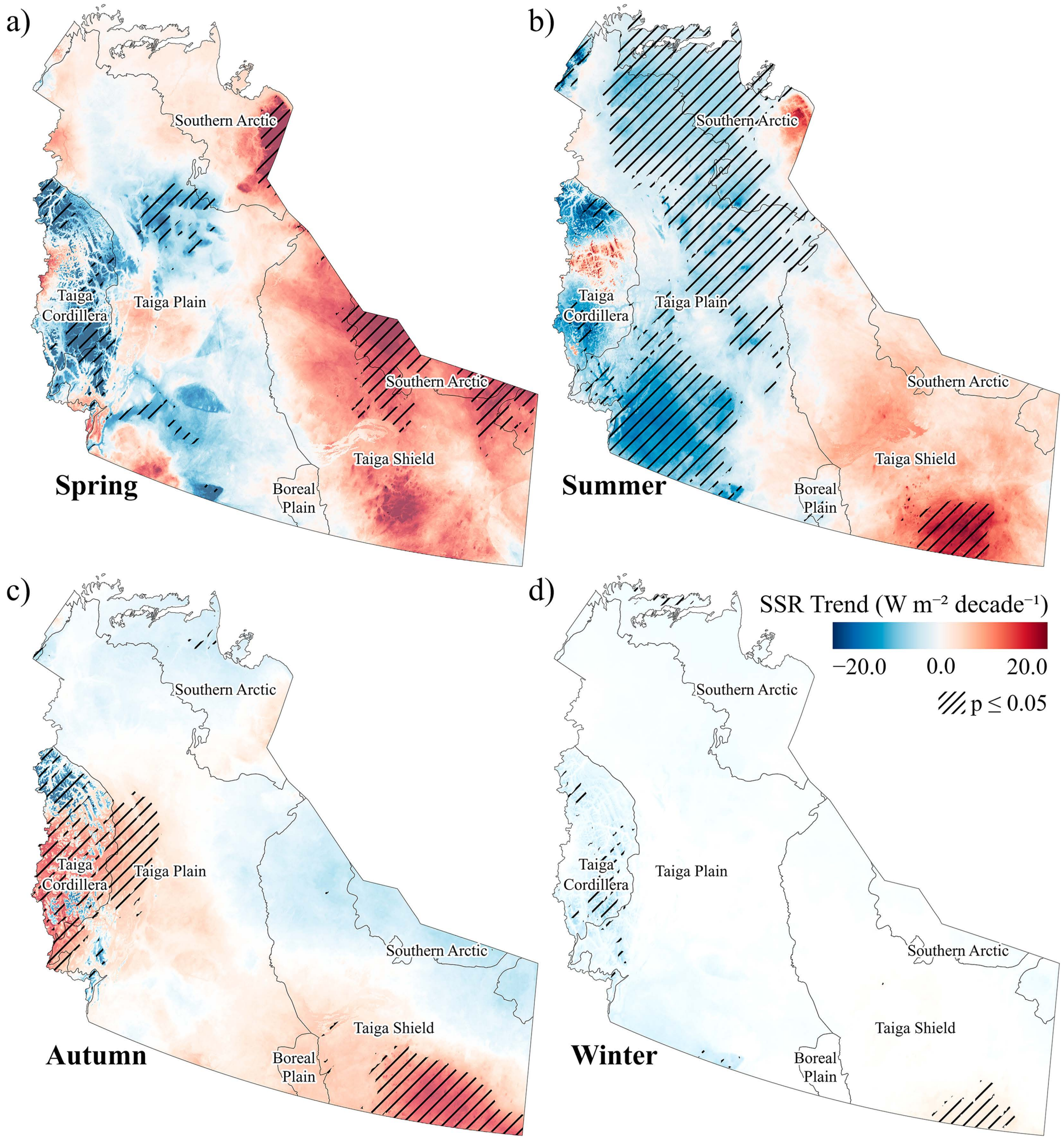

FIG. 4. Spatial distribution of seasonal SSR trends across the NWT for (a) spring (March–May), (b) summer (June–August), (c) autumn (September–November), and (d) winter (December–February). Trends were derived from mean seasonal Daymet SSR data (native resolution: ~1 km) using the MK test over the 1980–2023 period. The color bar ($\mathrm{W\ m^{-2}\ decade^{-1}}$) represents the rate of change (Sen's slope), while shaded areas denote statistically significant trends ($p \leq 0.05$).

periods (Weston et al. 2007; Wild 2009; Sanchez-Lorenzo et al. 2015; Yuan et al. 2021). Below, we discuss some potential causes of the observed spatiotemporal patterns in SSR trends and the implications of warming LSWT on northern communities and lake ecosystem condition.

a. Causes of observed changes in SSR trends

Long-term SSR trends have been attributed to various drivers of change within Earth's climate system (Wild 2009; Chiacchio et al. 2010; Huang et al. 2019). These drivers include changes in radiatively reactive gases in the atmosphere, such as water vapor, changes in aerosol levels, reduction in Arctic Sea ice, variation in atmospheric–oceanic circulation patterns (e.g., North Atlantic Oscillation, Pacific decadal oscillation), and changes in cloud characteristics (Wild 2009; Chiacchio et al. 2010; Huang et al. 2019; Augustine and Capotondi 2022; Chtirkova et al. 2023). Yuan et al. (2021) found that cloud cover and diurnal temperature range are the two most important variables in predicting long-term SSR changes globally. It is expected that an increase in daytime SSR would lead to a greater difference between daytime maximum and nighttime minimum temperatures (Bristow and Campbell 1984). Thus, trends in the diurnal temperature range can be used as a proxy for SSR trends (Bristow and Campbell 1984).

TABLE 2. Statistics of the mean seasonal Daymet SSR (Sen's slope; W m^{-2} $decade^{-1}$) trend magnitude across the NWT and its ecozones over the analyzed periods. These values are the averages of the pixel trends within each ecozone (NA = northern Arctic; SA = southern Arctic; TC = Taiga Cordillera; TP = Taiga Plain; TS = Taiga Shield; BC = Boreal Cordillera; BP = Boreal Plain; NWT = Northwest Territories). Values in parentheses indicate the range (minimum, maximum) of pixel slopes within each ecozone, and values in square brackets indicate the percentage of each ecozone's area where the trend is statistically significant ($p \leq 0.05$).

	NA	SA	TC	TP	TS	BC	BP	NWT
Area (km^2)	2351	175 257	83 819	511 664	343 222	5102	16 728	1 138 142
Spring	0.4	0.9	−2.4	−0.7	1.0	−0.5	−0.2	−0.1
(1980–2023)	(0.2, 0.5)	(−2.8, 6.0)	(−20.6, 3.1)	(−16.2, 3.4)	(−1.5, 4.5)	(−11.8, 2.5)	(−1.5, 0.5)	(−20.6, 6.0)
	[0%]	[26%]	[26%]	[6%]	[8%]	[6%]	[0%]	[12%]
Summer	−2.1	−1.5	−2.8	−2.6	0.4	−2.6	−1.3	−1.6
(1980–2023)	(−2.4, −1.7)	(−6.8, 4.5)	(−14.2, 10.2)	(−8.9, 0.8)	(−2.6, 6.6)	(−5.3, −0.3)	(−3.2, 0.9)	(−14.2, 10.2)
	[0%]	[52%]	[16%]	[54%]	[8%]	[28%]	[8%]	[36%]
Autumn	−0.5	−0.3	0.3	0.2	0.3	0.3	1.0	0.2
(1980–2023)	(−0.6, −0.3)	(−1.2, 1.0)	(−7.6, 3.2)	(−3.5, 2.7)	(−1.1, 3.1)	(−3.9, 2.2)	(0.6, 1.2)	(−7.6, 3.2)
	[0%]	[1%]	[58%]	[7%]	[16%]	[43%]	[1%]	[13%]
Winter	−0.1	0.0	−0.3	0.0	0.2	−0.2	0.2	0.0
(1980–2023)	(−0.1, −0.1)	(−0.3, 0.3)	(−1.8, 0.4)	(−1.3, 0.4)	(−0.2, 1.1)	(−1.4, 0.1)	(−0.1, 0.3)	(−1.8, 1.1)
	[0%]	[2%]	[17%]	[1%]	[4%]	[5%]	[0%]	[3%]

A long-term decrease in the diurnal temperature range has been observed in Canada since 1950, which has been attributed to increases in cloud cover (Vincent and Mekis 2006). Milewska (2004) showed that TCC in NWT increased from 3% to 9% between 1953 and 2002. The results of this study align with earlier findings, indicating a negative relationship between cloud cover and SSR from 1980 to 2023 (Fig. 7). This relationship is consistent with known relationships between cloud cover and SSR (Twomey 1976; Zhang et al. 1996; Kejna et al. 2021), particularly during the summer (Figs. 6 and 7b) when SSR reaches its maximum (Box et al. 2019). Additionally, a recent modeling study by Dong et al. (2023) concluded that changes in anthropogenic aerosol emissions, greenhouse gas concentrations, sea surface temperature, and sea ice extent contributed to observed decadal trends in SSR patterns over North America. The authors identified changes in sea surface temperature and sea ice extent as primary drivers of cloud-cover trends and SSR (Dong et al. 2023). Similarly, the observed sea ice reduction and prolonged periods of open water in the Beaufort Sea and in the Mackenzie River basin (Duguay et al. 2006; Box et al. 2019; Heo et al. 2021) may have resulted in increased local TCC, leading to reduced SSR in the northern Taiga Plains and northern Arctic ecozones (Figs. 3 and 4). The Taiga Cordillera ecozone exhibits the largest range of annual-mean SSR across all NWT ecozones, as highlighted in Fig. A5, driven by its mountainous terrain of high average elevation (1394 m) and dynamic atmospheric conditions, including high wind speeds (Prowse et al. 2009; Garibaldi et al. 2022). These factors may contribute to significant SSR fluctuations, resulting in opposing 1980–2000 and 2001–23 trends (Figs. 3a,b). The complexity of interpreting SSR patterns in the Taiga Cordillera underscores the limitations of statistical significance tests such as the MK test in regions with substantial variability and heterogeneity. However, exploring this in more detail is beyond the scope of the present study.

b. *Variability of LSWT in relation to SSR*

Results indicate a general decrease in incident summer SSR in the North Slave Region between 1984 and 2020 (Fig. 8a). However, during the same period, summer LSWT exhibited an increase of +1.2 to +4.6°C (Fig. 8b), which is substantial relative to the mean and median LSWT of −1.6° and −1.7°C, respectively, potentially affecting their thermal regimes through increased evaporation rates (Rouse et al. 2005). Consequently, it is possible that increased evaporation has contributed to elevated amounts of local TCC and a subsequent decrease in SSR (Figs. 6 and 7) (Hu et al. 2017). The difference in the direction of the correlation between LSWT and SSR in summer in medium and large lakes (negative correlation) versus in small lakes (positive correlation) is likely driven by the higher heat capacity of medium and large lakes, which make them less sensitive to changes in SSR (Bailey et al. 1997). Mechanical mixing by wind in medium and large lakes (Rouse et al. 2005) can cause cooler subsurface water to mix with warmer upper lake water, leading to a slower heating process compared to small lakes and resulting in a delay of the spring release of latent and sensible heat fluxes (Rouse et al. 2005). Additionally, recent studies highlight that large and deep lakes demonstrate a lagged thermal response to external forcings due to their high heat capacity and delayed onset of stratification (Woolway and Merchant 2017; Zhang et al. 2024). These lakes exhibit a longer thermal memory, often responding to changes in SSR over extended periods. This phenomenon has also been observed in cold-climate lakes, where interannual variations in stratification onset significantly influence LSWT during summer (Woolway et al. 2021). Conversely, small lakes, with lower thermal inertia, show rapid warming patterns due to direct solar inputs, indicated by positive correlations with SSR (Bailey et al. 1997; Woolway and Merchant 2017). For example, large lakes near the Central Mackenzie River basin in the NWT tend to lose heat and water vapor almost as quickly at night as during the day,

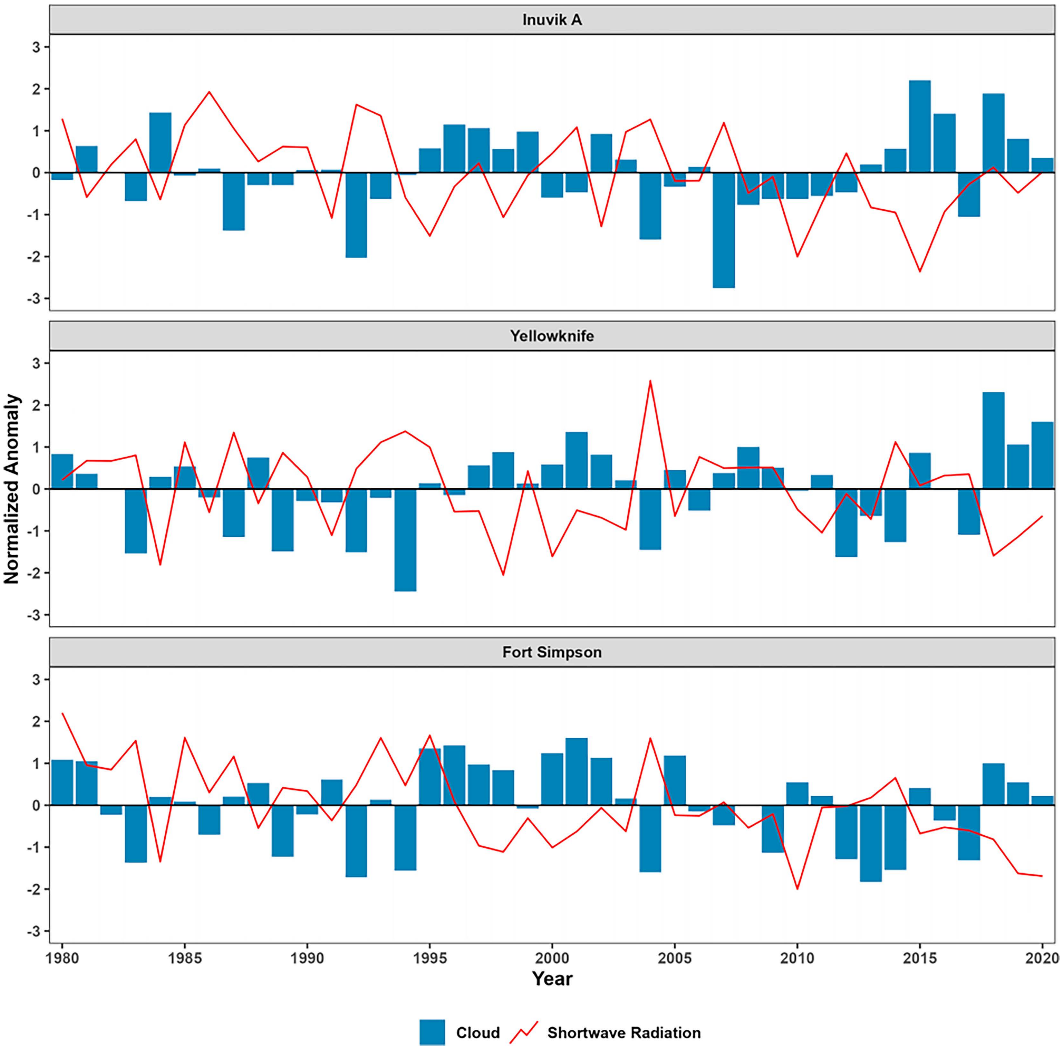

FIG. 5. Time series of mean summer values of normalized in situ TCC observations (blue bars) and Daymet SSR estimates (red lines) for three measurement locations (Inuvik, Yellowknife, and Fort Simpson) in the NWT over 1980–2020. The zero line represents the 1980–2020 long-term average.

particularly in late summer and autumn than in spring and early summer (Rouse et al. 2005). These large lakes are particularly sensitive to the surrounding air; a warm, calm, and sunny period may be followed by a cold, dry air mass with more cloudiness and windy conditions that can increase convection and latent heat energy, even without direct solar input (Rouse et al. 2005). The increased cloudiness can enhance SSR reflection at the top of the atmosphere, reducing the amount of SSR absorbed by Earth's surface. Additionally, clouds increase the emissivity of the atmosphere, leading to an increase in downward longwave radiation (Twomey 1976; Zhang et al. 1996). The higher longwave radiation input leads to decreased heat loss from lakes during nighttime (Livingstone 2003; Fink et al. 2014), potentially contributing to the observed warming of some of the lakes in the North Slave Region.

Additionally, the correlation between SSR and LSWT has a spatial pattern that appears to be consistent with the northern tree line boundaries (to be more accurate, the southern 50 km buffer from the tree line; see Fig. 9a). These boundaries are characterized by the transition of the boreal forest northward into tundra, approximating the summer position of the Arctic Front (Pienitz et al. 1997). The heating differences between boreal forest and tundra regions can drive localized circulations and have ecological implications (Beringer et al. 2001). Green et al. (2017) reported that the interactions between the atmosphere and vegetation can account for up to ~30% of variability in surface radiation and precipitation patterns due to the release of water vapor during photosynthesis. The lakes within the tundra region, governed by an open canopy, may allow SSR to penetrate more deeply (Bailey et al. 1997), leading to increased evaporation and cloud formation at the local level. These factors collectively may also affect SSR receipt and rapid changes in surface characteristics and microclimates at the local scale. However, further research is required to

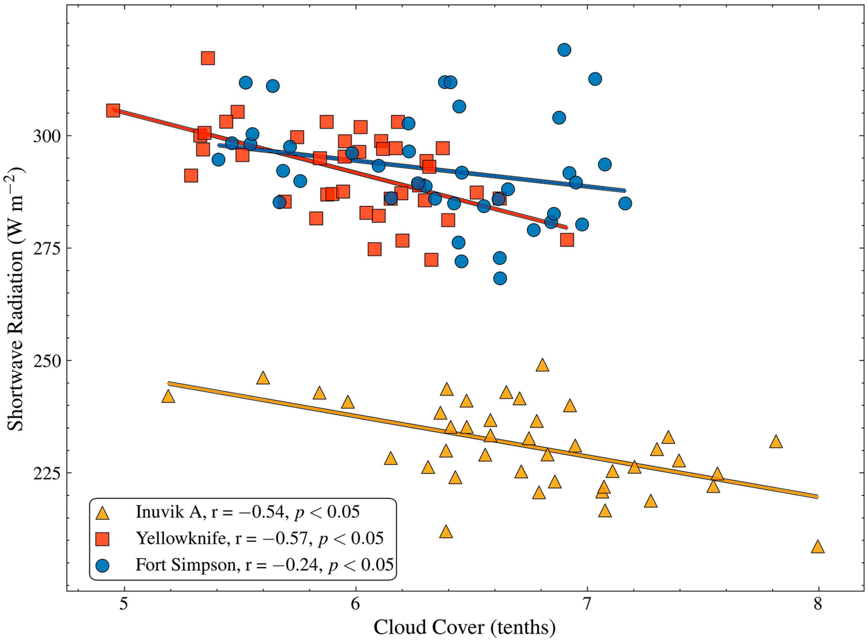

FIG. 6. Scatterplot showing relationship between mean summer values of in situ TCC observations and Daymet SSR for three measurement locations (Inuvik, Yellowknife, and Fort Simpson) in the NWT over 1980–2020.

confirm that the northern tree line is the primary control on changes in SSR trends and SSR–LSWT correlation.

c. *Implications of warming lakes for northern communities and ecosystems*

This study reveals that during summer, LSWT in the North Slave Region experienced an increase between 1984 and 2020, ranging from +1.2°C to +4.6°C in 45% of lakes (Fig. 9), as also reported by Attiah et al. (2023), which is consistent with global trends (O'Reilly et al. 2015). Future projections suggest an even higher lake temperature increase, with potential maxima reaching 30°C by 2100 (Sharma et al. 2007; Råman Vinnå et al. 2021). These long-term temperature changes may have implications for ice road construction and transportation networks in northern communities, as warming delays ice formation and affects ice road accessibility (Duguay et al. 2006; Levin 2017).

Furthermore, changes in SSR can influence lake conditions, particularly through its relationship with cloud cover. The observed negative correlation between TCC and SSR during the summer (Fig. 7b) highlights that increasing cloud cover reduces SSR, which can affect photosynthesis and lower dissolved oxygen concentrations in lakes (Twomey 1976; Zhang et al. 1996; Schindler et al. 1997; Kejna et al. 2021; Woolway et al. 2022). Additionally, water quality parameters such as turbidity play a significant role in SSR absorption, with lakes high in dissolved organic carbon attenuating more SSR. This can lead to enhanced stratification, potentially affecting fisheries and impacting communities that depend on these ecosystems for economic stability and food security (Adams et al. 2022; Pienitz et al. 1997; Molot et al. 2005; Pilla and Couture 2021; Sharma et al. 2007; Moslemi-Aqdam et al. 2022). While these interactions are critical to understanding the broader implications of SSR variability, they are beyond the scope of the present study. Future research should explore these ecological and socioeconomic dynamics in greater detail to fully understand the impacts on high-latitude lake systems.

d. *Use of gridded and remote sensing data, potential limitations, and opportunities*

This research used Daymet interpolated SSR, ERA5 reanalysis TCC, and Landsat-derived LSWT data to study their long-term trends and variability across the continental NWT. It is important to acknowledge that gridded interpolated and remote sensing data may introduce uncertainties, which can either amplify or underestimate trend magnitudes. For example, Daymet SSR estimates used in this study rely on limited in situ data, which can be challenging to obtain in northern regions (Thornton et al. 2021; GNWT 2018; Diaconescu et al. 2023). However, the use of gridded and remote sensing data allows researchers to detect and attribute changes over extensive spatial areas where in situ measurements are not readily available (Zhang et al. 2000; Derksen et al. 2008; Murfitt and Brown 2017).

While the dataset used in this study provides a reasonable quantification and insights into the spatiotemporal evolution of SSR and LSWT in unmonitored locations, it is important to note that more comprehensive investigations into cloud characteristics and other drivers of observed SSR trends are warranted. The relationship between SSR and LSWT is complex and influenced by factors such as catchment geology and

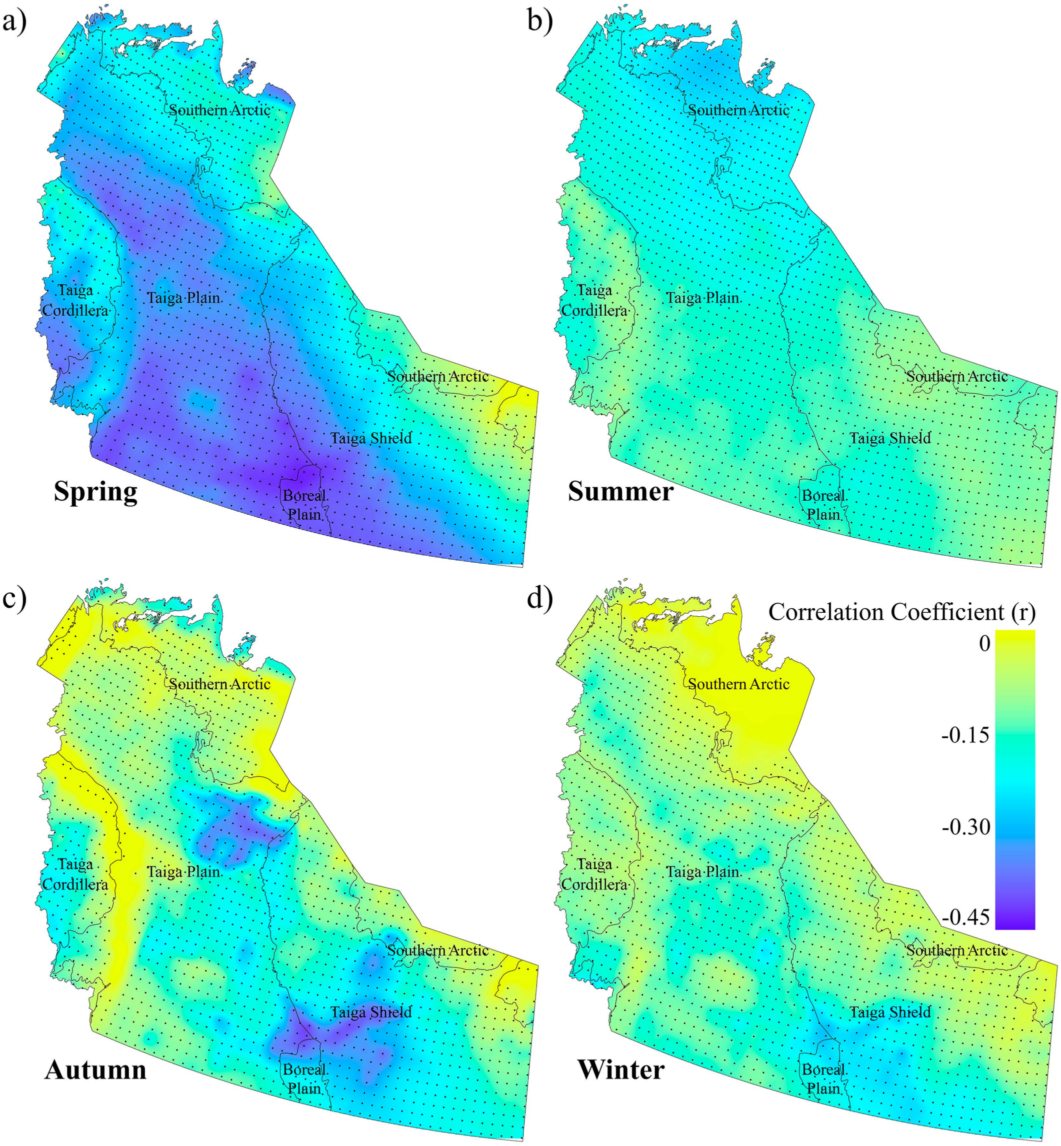

FIG. 7. Seasonal Pearson's correlation coefficient r between ERA5 daily TCC and Daymet daily SSR matchups (corresponding pixels) over the NWT from 1980 to 2023 displayed for (a) spring (March–May), (b) summer (June–August), (c) autumn (September–November), and (d) winter (December–February). Black dots indicate grid points where Pearson's correlation coefficients are statistically significant at $p \leq 0.05$.

soil type, geographic region, topography, aspect and vegetation, and local climate conditions (Bigras 1990; O'Reilly et al. 2015; Thompson et al. 2020). In-depth studies considering these factors and their interactions would require in situ investigations and long-term data collection. Nevertheless, this research contributes to the understanding of SSR–LSWT relationships by examining a large number of lakes of various sizes over an extended period of nearly four decades (1984–2020), in contrast to previous studies that focused on a limited number of lakes over shorter time frames (e.g., Oswald and Rouse 2004; Rouse et al. 2005). Furthermore, the analysis identified the significant influence of lake size on the sensitivity of SSR and LSWT during the same period.

6. Conclusions

This study improves our understanding of long-term historical trends and patterns of SSR receipt across the continental NWT as derived from Daymet SSR interpolated data, ERA5 TCC data from ECMWF, and explored linkages between SSR and LSWT in the North Slave Region using Landsat remotely sensed data. Key findings are summarized below:

1) From 1980 to 2023, annual SSR decreased in most northwestern ecozones, including the Taiga Cordillera and Taiga Plains, while a generally positive trend was observed in southeastern ecozones such as the Taiga Shield. The highest rate of change was observed in the Taiga Cordillera

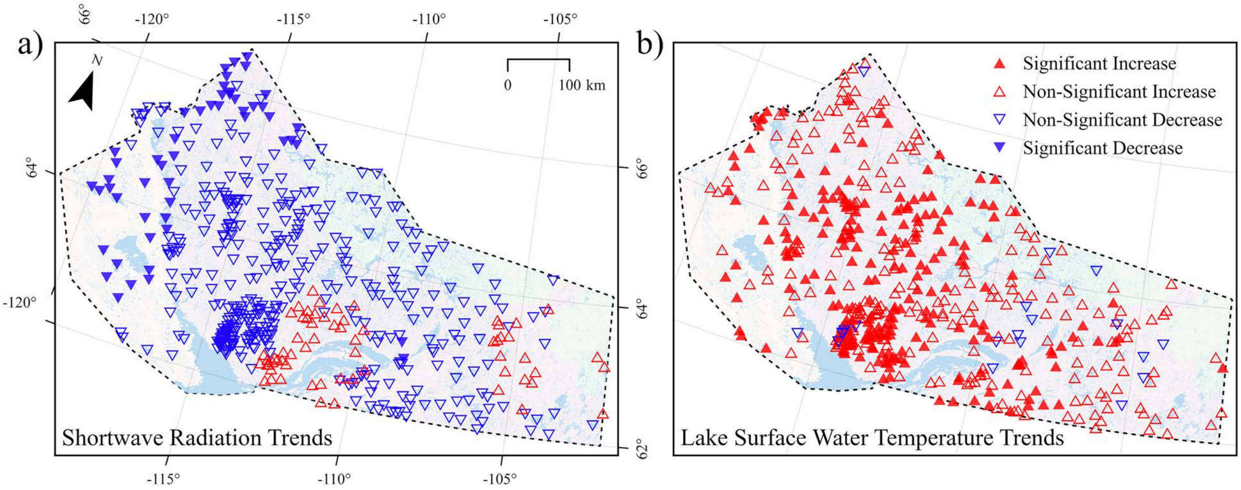

FIG. 8. MK trend analysis of mean summer values for (a) Daymet SSR and (b) LSWT over the North Slave Region from 1984 to 2020. Solid red and blue triangles indicate statistically significant (increasing and decreasing, respectively) trends at $p \leq 0.05$, while open triangles represent nonsignificant trends.

ecozone. SSR trends in the Taiga Shield and Boreal Plain ecozones typically decreased from 1980 to 2000 and increased from 2001 to 2023, contrasting with the Taiga Cordillera ecozone where SSR increased prior to 2000 and declined thereafter.

2) Seasonally, SSR trends showed varying but distinct patterns across ecozones from 1980 to 2023. In spring, increasing trends were observed in the Taiga Shield (average rate of change $+1.0$ W m^{-2} decade^{-1}) and southern Arctic ($+0.9$ W m^{-2} decade^{-1}) ecozones. In contrast, summer SSR showed a general reduction with an average rate of change of -1.6 W m^{-2} decade^{-1} across the entire NWT, with the largest declining rates in the Taiga Plain (-2.6 W m^{-2} decade^{-1}), Taiga Cordillera (-2.8 W m^{-2} decade^{-1}), and Boreal Cordillera (-2.6 W m^{-2} decade^{-1}) ecozones.
3) There was a negative correspondence between SSR receipt and cloud cover, particularly during the spring months. This relationship aligns with previous research on the cloud–climate interaction over the Arctic region.
4) Small lakes showed a positive correlation between LSWT and incoming SSR, whereas the majority of medium and

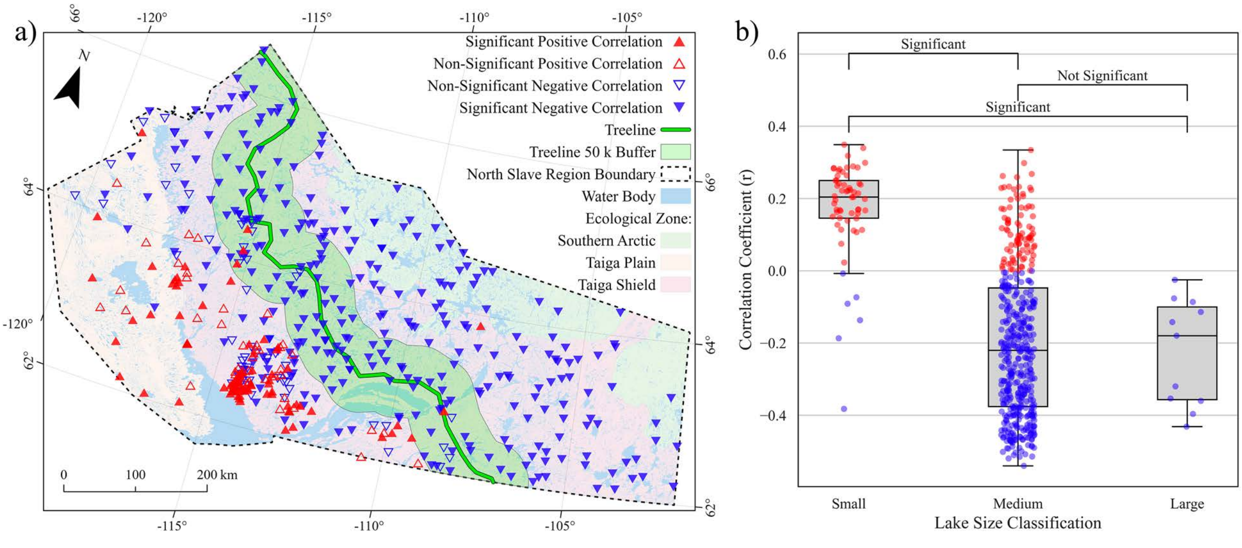

FIG. 9. (a) Spatial distribution of Pearson's correlation coefficients between mean summer Daymet SSR and Landsat-derived LSWT from 1984 to 2020 for over 500 lakes in the North Slave Region. Blue markers represent negative correlations, and red markers represent positive correlations; solid symbols denote statistically significant correlations ($p \leq 0.05$), and hollow symbols denote nonsignificant correlations. The green line shows the tree line, and the lightly shaded buffer illustrates a 50-km zone around it. (b) Boxplots of the derived Pearson correlation coefficients (blue = negative and red = positive) categorized by lake size: small (<1 km^2; $n = 62$), medium (1–100 km^2; $n = 464$), and large (>100 km^2; $n = 12$). Brackets above the boxes indicate pairwise independent two-sample Student's t tests between size classes that are significant at $p \leq 0.05$.

large lakes exhibited a negative correlation. The implications of persistent lake warming and changing SSR on northern communities and lake ecosystems were discussed.

5) The use of gridded and remote sensing data in this study highlights their value in advancing understanding of how water temperatures of northern lakes are changing.

Together, these findings provide new insights into the changing trends over the past 44 years in the NWT, a period characterized by significant atmospheric warming. They also underscore the implications of these changes on lake-rich regions in NWT, which play a crucial role in the Earth system. However, the heterogeneity in long-term trends in SSR receipt across NWT emphasizes the need to consider interactions among climate variables at different spatiotemporal scales. Monitoring mechanisms for tracking changing lake behavior remain crucial for researchers and decision-makers because lake data are essential to support weather, climate, and hydrological predictions. To the best of our knowledge, this work also represents one of the first attempts to quantitatively examine long-term SSR trends while relating the changes to cloud cover using Daymet and ERA5 data during a four-decade period (1980–2023) in the continental NWT. Thus, it can serve as a benchmark for policymakers when synthesizing future climate reports for northern regions.

Acknowledgments. We are grateful to the Global Water Futures Programme for providing access to their research facilities that are supported by the Canada First Research Excellence Fund, which helped with this study's completion. Thanks to Ariel Lisogorsky for his guidance with programming. Special thanks are extended to Julie Grant for her valuable contributions to the figure's aesthetics, as well as to Stephanie Slowinski and Dr. Chris Derksen for their insightful inputs on an earlier version of this manuscript. We also extend our gratitude to the four anonymous reviewers for their time and valuable feedback, which helped improve this manuscript.

Data availability statement. Daymet SSR data were downloaded from https://daac.ornl.gov/cgi-bin/dsviewer.pl?ds_id=2129, while Landsat-derived LSWT data are available from https://doi.org/10.5683/SP3/J4GMC2. In situ cloud-cover observations for Inuvik, Fort Simpson, and Yellowknife were collected from Environment and Climate Change Canada (ECCC). ERA5 TCC data were downloaded from the Copernicus Data Hub at https://cds.climate.copernicus.eu/datasets/reanalysis-era5-single-levels. CERES solar insolation data can be accessed via https://ceres.larc.nasa.gov/data/, and MODIS cloud fraction data (MODIS level-3 cloud properties) are available for download at https://search.earthdata.nasa.gov/ or https://ladsweb.modaps.eosdis.nasa.gov/search/. All data and analysis code for this study (excluding raw data accessible from the links above) are publicly available at the FRDR repository at https://doi.org/10.20383/103.01165.

APPENDIX

Supplementary Materials

a. Technical validation of Daymet SSR and ERA5 TCC data with CERES and MODIS remote sensing data

Before conducting our main analyses, we performed a series of validations to assess the reliability and suitability of the

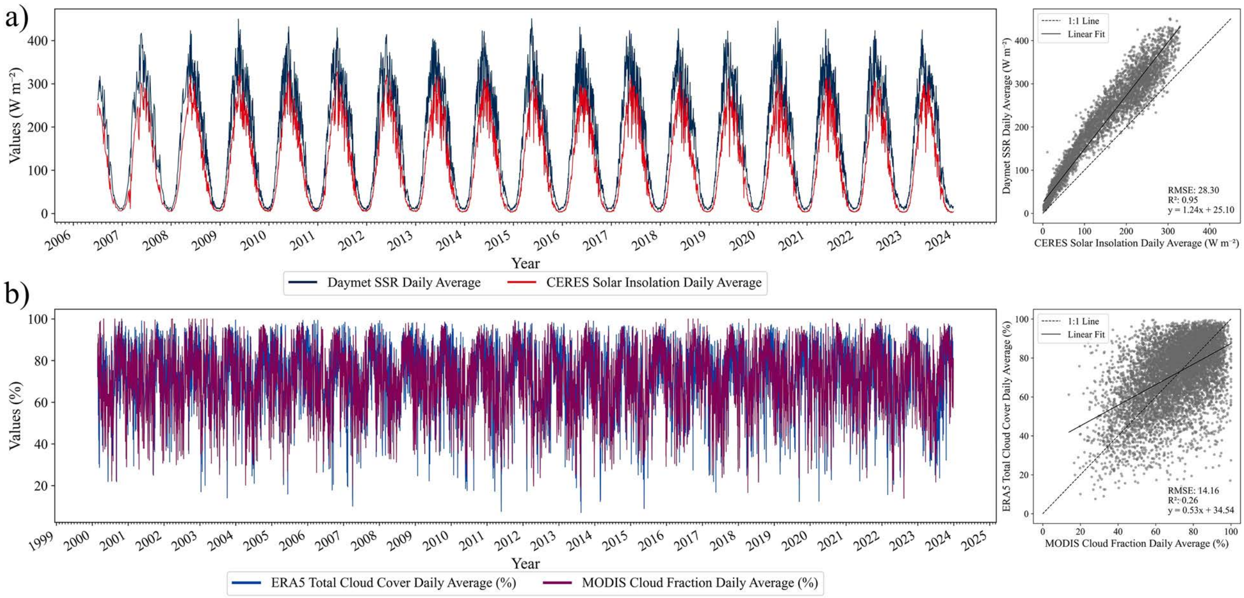

FIG. A1. Intercomparisons of (a) Daymet daily SSR and CERES daily solar insolation data from 2006 to 2024 and (b) ERA5 daily TCC and MODIS daily cloud fraction from 2000 to 2024. The left panels present a time series of daily averages spatially averaged over the NWT for the longest available comparable period. (right) Scatterplots showing one-to-one relationships, where a 1:1 line indicates perfect agreement. The linear regression slope, RMSE, and R^2 values assess the agreement and validity of the datasets used in this study with remote sensing–based data.

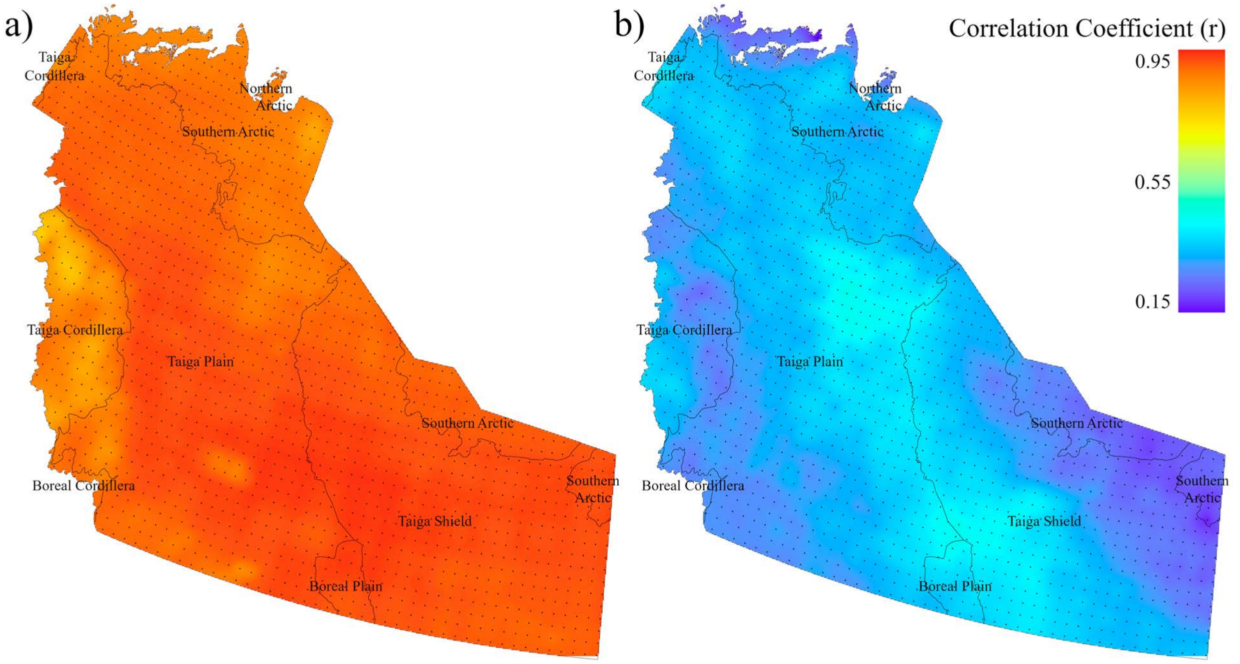

Daymet SSR and CERES Solar Insolation (2006-2024)

ERA 5 Total Cloud Cover and MODIS Cloud Fraction (2000-2024)

FIG. A2. Pearson's correlation coefficient r for (a) Daymet daily SSR and CERES daily solar insolation matchups (corresponding pixels) from 2006 to 2024 and (b) ERA5 daily TCC and MODIS daily cloud fraction matchups from 2000 to 2024 over the NWT. Black dots indicate grid points where correlation coefficients are statistically significant ($p \leq 0.05$).

Daymet SSR and ERA5 TCC datasets for the methodology. Given the limited availability of in situ measurements, particularly for SSR, these validation steps ensure that our chosen data products align with independent remote sensing–based datasets and capture the underlying variability at appropriate temporal and spatial scales.

To evaluate the accuracy of Daymet SSR, we compared it with NASA's Clouds and the Earth's Radiant Energy System (CERES) daily solar insolation data (Fig. A1a). The CERES instrument provides top-of-the-atmosphere (TOA) radiative flux measurements, which are then converted to surface solar insolation estimates using a well-established radiative transfer methodology (Wielicki et al. 1996). Temporal comparisons reveal that Daymet SSR and CERES solar insolation exhibit highly similar seasonal and interannual patterns, demonstrating consistent peaks and troughs throughout the studied period (2006–24). Despite a slight positive bias in Daymet SSR (notably at high values), the linear regression analysis indicates a strong agreement, with an R^2 value of 0.95. This near-perfect temporal alignment and the relatively low RMSE underscore the robustness of Daymet SSR estimates in representing the temporal variability of incoming SSR over the NWT. Spatially, a point-by-point (on a common grid mesh) Pearson's correlation analysis between Daymet SSR and CERES solar insolation matchups (corresponding pixels) also confirms this strong alignment (Fig. A2a). Most areas exhibit statistically significant correlations ($p \leq 0.05$), indicating that Daymet captures the spatial distribution of SSR variations well, even in a region with sparse ground-based radiometric measurements. These results provide confidence that Daymet SSR can reliably serve as the primary input for long-term trend analyses in this study.

For cloud cover, we compared ERA5 daily TCC data with the MODIS (from both *Terra* and *Aqua* satellites) daily cloud fraction product over the 2000–24 period (Fig. A1b). MODIS cloud fraction, derived at 1-km resolution from level-3 cloud properties products and first collected by the *Terra* satellite launched in 1999, offers a detailed view of cloud variability but spans a shorter historical period than ERA5. The time series comparison shows that while both ERA5 and MODIS capture general cloud-cover dynamics—the one-to-one scatter closely aligns with the perfect fit, demonstrating fair representation of the regionwide mean behavior—the relationship is more moderate, yielding an R^2 value of about 0.26. This lower agreement can be attributed to several factors. First, MODIS provides a finer spatial and temporal depiction of cloud heterogeneity—via instantaneous 1-km overpass snapshots—potentially capturing transient and localized cloud events not resolved by the coarser ERA5 grid (~31 km). Second, differences in retrieval algorithms and underlying assumptions (e.g., atmospheric profiles, cloud overlap assumptions, and spectral thresholding) may introduce systematic discrepancies (Ackerman et al. 1998; Dee et al. 2011).

It is worth noting that ERA5 TCC is a model-based reanalysis that ingests hourly observations into a multilayer overlap scheme and then aggregates them to daily means, smoothing out short-term variability and reducing direct comparability to

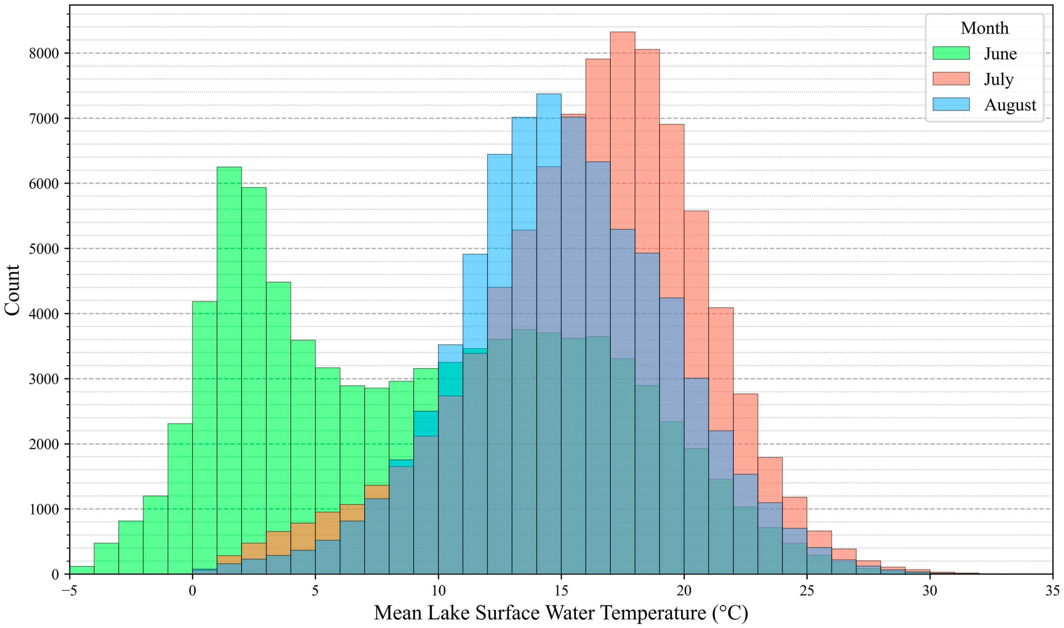

FIG. A3. Histogram distributions of mean LSWT (°C) for the summer months of June (green), July (red), and August (blue). The y axis shows the count of lake temperature instances. Temperature means were calculated over all retrieved pixels of each lake. Distributions are based on daily Landsat-derived LSWT estimates for over 500 lakes in the North Slave Region covering 1984–2021 based on the work of Attiah et al. (2023).

the instantaneous satellite snapshots of MODIS. Despite these differences, the long-term, regionwide behavior remains consistent: The one-to-one comparison (Fig. A1b) follows the 1:1 line fairly (RMSE ≈ 14%), and the spatial correlation patterns in Fig. A2b, while moderate (ranging from 0.15 to 0.50), remain statistically significant ($p \le 0.05$) over the majority of the study area. Given the paucity of in situ cloud observations across the NWT—and the need for a continuous daily time series spanning 2000–24—MODIS represents the most spatially detailed sensor alternative to ERA5 for validation, even if their native sampling schemes cannot be perfectly synchronized.

b. Distribution of Landsat-derived mean lake surface water temperature records

Figure A3 summarizes the daily lakewide mean surface temperatures retrieved from the thermal bands of Landsat 5, 7, and 8 across more than 500 lakes in the North Slave Region [based on the work of Attiah et al. (2023)]. In total, 245 187 summer records (June–August) were analyzed: 34% in June, 35% in July, and 31% in August.

c. Yearly distribution of Daymet SSR

Figure A4 depicts annual-mean Daymet SSR over NWT from 1980 to 2023 using a ridgeline plot. This visualization arranges kernel density estimates (KDEs) of the annual-mean SSR data vertically stacked, allowing for a clear year-to-year comparison. The KDE, by default employing a Gaussian kernel, transforms discrete data samples into a continuous probability density function, thereby smoothing out random fluctuations and highlighting the overall distributional shape. We also applied the Shapiro–Wilk (SW) normality test to each year's SSR distribution. The SW test is a widely accepted method to assess how closely a dataset follows a normal distribution, with test statistics closer to 1 signaling greater normality. Across years, SW statistics exceeded 0.93, consistent with near-normal distributions; together with the KDE shapes in Fig. A4, this supports treating annual-mean SSR as approximately Gaussian.

d. SSR trend analysis (linear)

Figure A5 presents the annual-mean Daymet SSR time series for seven ecozones within NWT from 1980 to 2023. The shaded areas highlight the observed maximum and minimum ranges across each year, illustrating the variability within these ecozones through the analyzed years. A vertical split line at the year 2000 marks a temporal breakpoint, distinguishing two distinct periods for trend evaluation. The linear trend lines calculated for the 1980–2000 and 2001–23 intervals reveal that, in five of the seven ecozones, the direction of the trend is reversed following the year 2000. This pattern supports the choice of 2000 as a meaningful breakpoint for analyzing long-term SSR trends in the NWT.

e. Correlation between total cloud cover and shortwave radiation

Figure A6 presents Pearson's r between ERA5 daily TCC and corresponding Daymet daily SSR pixel value across NWT for the entire 1980–2023 period. Black dots indicate grid points where the correlations are statistically significant ($p \le 0.05$),

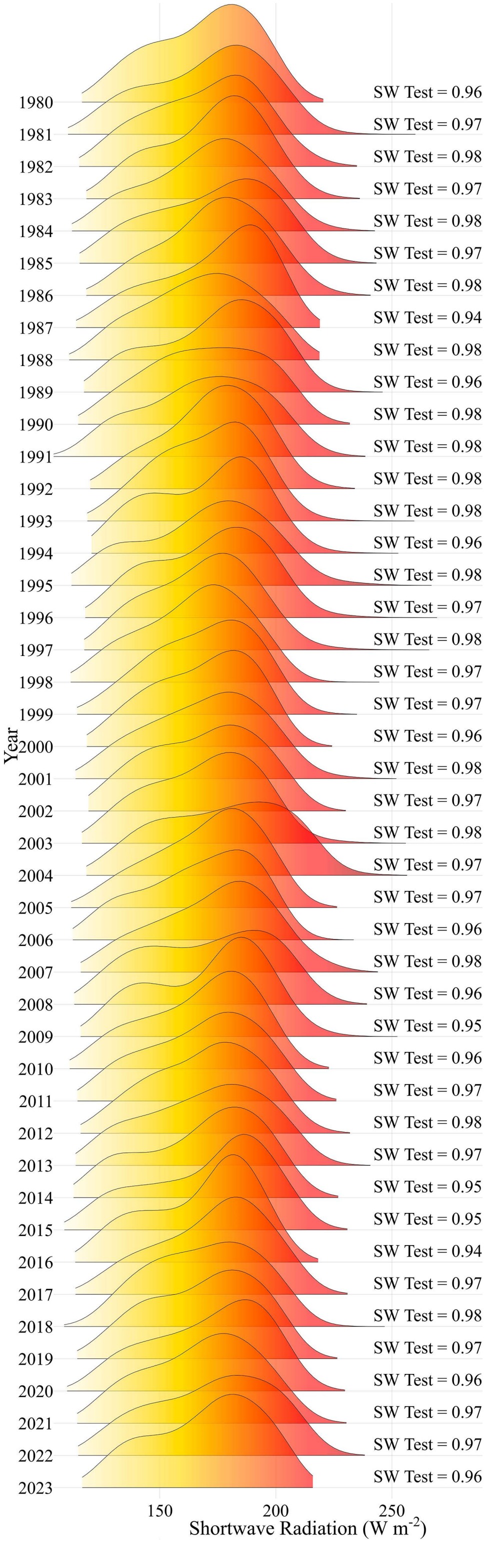

FIG. A4. Ridgeline plot of annual-mean Daymet SSR over the NWT from 1980 to 2023. Each colored curve represents a KDE of the annual-mean SSR distribution, where the KDE is computed using a Gaussian kernel approximating the underlying frequency distribution of the data. The reported SW test results indicate a statistically significant approximation to normality for these distributions.

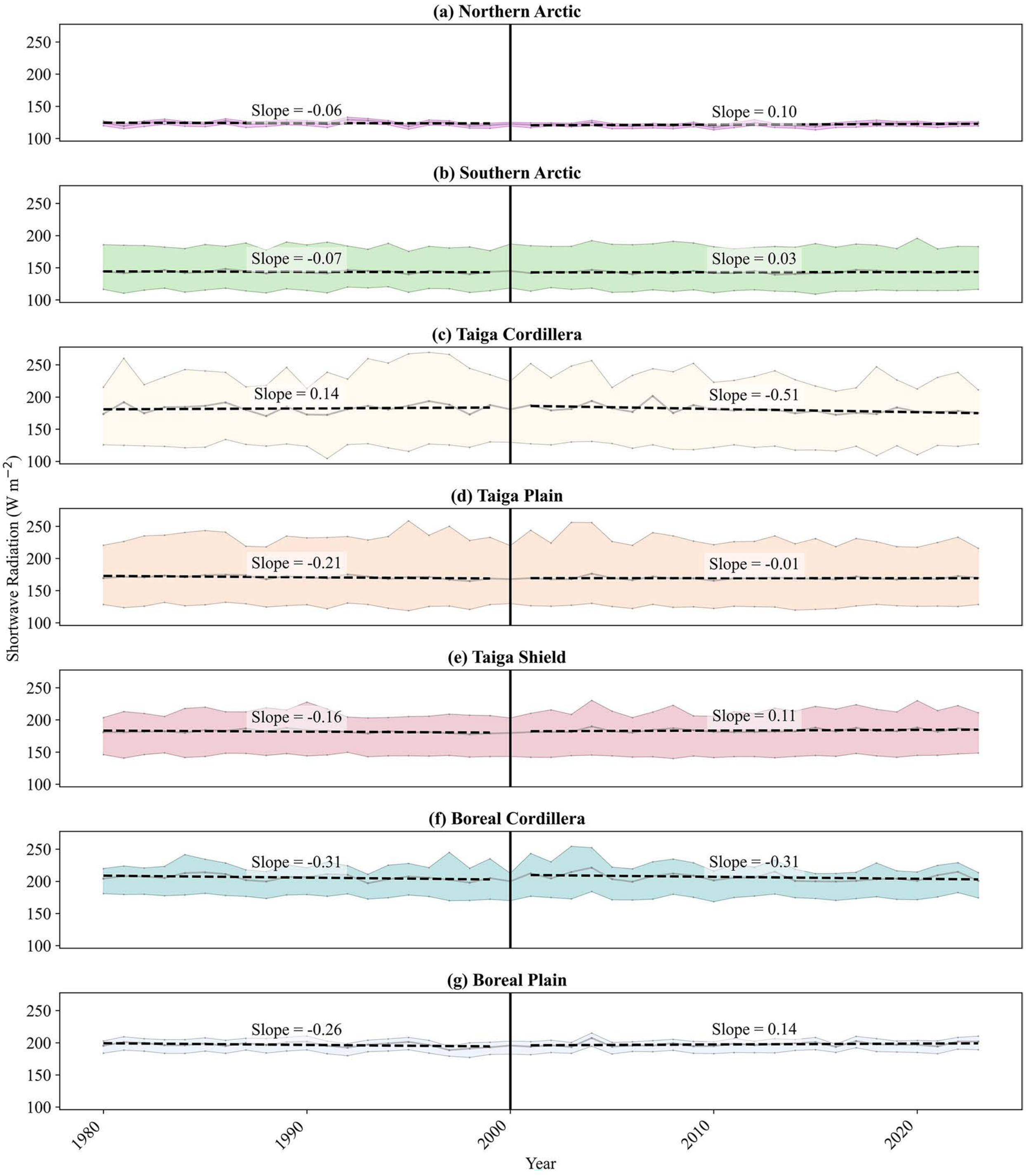

FIG. A5. Time series of annual-mean Daymet SSR values (W m^{-2}) for seven ecozones in the NWT from 1980 to 2023. Each ecozone [for (a) northern Arctic, (b) southern Arctic, (c) Taiga Cordillera, (d) Taiga Plain, (e) Taiga Shield, (f) Boreal Cordillera, and (g) Boreal Plain] is color coded, displaying the range of variation (maximum, average, and minimum) within each zone. The dashed black lines indicate trends for the 1980–2000 and 2001–23 periods, with the slope (W m^{-2} yr^{-1}) of the (linear) trend displayed on each line.

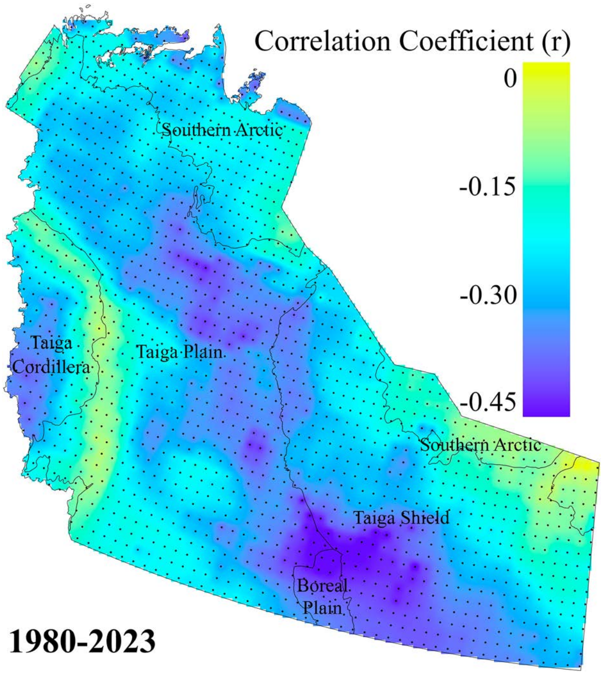

FIG. A6. Correlation coefficient r between ERA5 daily TCC and Daymet daily SSR matchups (corresponding pixels) over the NWT from 1980 to 2023. Black dots indicate grid points where correlation coefficients are statistically significant at $p \leq 0.05$.

providing a spatial overview of how TCC and SSR are related throughout the region.

REFERENCES

Abe, M., T. Nozawa, T. Ogura, and K. Takata, 2016: Effect of retreating sea ice on Arctic cloud cover in simulated recent global warming. *Atmos. Chem. Phys.*, **16**, 14 343–14 356, https://doi.org/10.5194/acp-16-14343-2016.

Ackerman, S. A., K. I. Strabala, W. P. Menzel, R. A. Frey, C. C. Moeller, and L. E. Gumley, 1998: Discriminating clear sky from clouds with MODIS. *J. Geophys. Res.*, **103**, 32 141–32 157, https://doi.org/10.1029/1998JD200032.

Adams, H., J. Ye, B. D. Persaud, S. Slowinski, H. Kheyrollah Pour, and P. Van Cappellen, 2022: Rates and timing of chlorophyll-*a* increases and related environmental variables in global temperate and cold-temperate lakes. *Earth Syst. Sci. Data*, **14**, 5139–5156, https://doi.org/10.5194/essd-14-5139-2022.

Adrian, R., and Coauthors, 2009: Lakes as sentinels of climate change. *Limnol. Oceanogr.*, **54**, 2283–2297, https://doi.org/10.4319/lo.2009.54.6_part_2.2283.

AMAP, 2021: Arctic Monitoring and Assessment Programme (AMAP) Arctic climate change update 2021: Key trends and impacts. Arctic Monitoring and Assessment Programme (AMAP), 148 pp., https://www.amap.no/documents/download/6890/inline.

Arias, P. A., and Coauthors, 2021: Technical summary. *Climate Change 2021: The Physical Science Basis*, V. Masson-Delmotte et al., Eds., Cambridge University Press, 33–144, https://doi.org/10.1017/9781009157896.002.

Attiah, G., H. Kheyrollah Pour, and A. K. Scott, 2023: Lake surface temperature retrieved from landsat satellite series (1984 to 2021) for the North Slave Region. *Earth Syst. Sci. Data*, **15**, 1329–1355, https://doi.org/10.5194/essd-15-1329-2023.

Augustine, J. A., and A. Capotondi, 2022: Forcing for multidecadal surface solar radiation trends over Northern Hemisphere continents. *J. Geophys. Res. Atmos.*, **127**, e2021JD036342, https://doi.org/10.1029/2021JD036342.

Bailey, W. G., T. R. Oke, and W. R. Rouse, 1997: *The Surface Climates of Canada.* McGill-Queen's Press University Press, 369 pp.

Beringer, J., N. J. Tapper, I. McHugh, F. S. Chapin III, A. H. Lynch, M. C. Serreze, and A. Slater, 2001: Impact of Arctic treeline on synoptic climate. *Geophys. Res. Lett.*, **28**, 4247–4250, https://doi.org/10.1029/2001GL012914.

Bigras, S. C., 1990: Hydrological regime of lakes in the Mackenzie Delta, Northwest Territories, Canada. *Arct. Alp. Res.*, **22**, 163–174, https://doi.org/10.1080/00040851.1990.12002778.

Box, J. E., and Coauthors, 2019: Key indicators of Arctic climate change: 1971–2017. *Environ. Res. Lett.*, **14**, 045010, https://doi.org/10.1088/1748-9326/aafc1b.

Bristow, K. L., and G. S. Campbell, 1984: On the relationship between incoming solar radiation and daily maximum and minimum temperature. *Agric. For. Meteor.*, **31**, 159–166, https://doi.org/10.1016/0168-1923(84)90017-0.

Budyko, M. I., 1969: The effect of solar radiation variations on the climate of the Earth. *Tellus*, **21A**, 611–619, https://doi.org/10.3402/tellusa.v21i5.10109.

Bush, E., and D. S. Lemmen, 2019: Canada's climate change report. Government of Canada, 444 pp., https://changingclimate.ca/CCCR2019/.

Chasmer, L., and C. Hopkinson, 2017: Threshold loss of discontinuous permafrost and landscape evolution. *Global Change Biol.*, **23**, 2672–2686, https://doi.org/10.1111/gcb.13537.

Chiacchio, M., T. Ewen, M. Wild, and E. Arabini, 2010: Influence of climate shifts on decadal variations of surface solar radiation in Alaska. *J. Geophys. Res.*, **115**, D00D21, https://doi.org/10.1029/2009JD012533.

Chtirkova, B., D. Folini, L. F. Correa, and M. Wild, 2023: Internal variability of the climate system mirrored in decadal-scale trends of surface solar radiation. *J. Geophys. Res. Atmos.*, **128**, e2023JD038573, https://doi.org/10.1029/2023JD038573.

Connon, R. F., W. L. Quinton, J. R. Craig, and M. Hayashi, 2014: Changing hydrologic connectivity due to permafrost thaw in the lower Liard River Valley, NWT, Canada. *Hydrol. Processes*, **28**, 4163–4178, https://doi.org/10.1002/hyp.10206.

Cutforth, H. W., and D. Judiesch, 2007: Long-term changes to incoming solar energy on the Canadian prairie. *Agric. For. Meteor.*, **145**, 167–175, https://doi.org/10.1016/j.agrformet.2007.04.011.

DeBeer, C. M., and Coauthors, 2021: Summary and synthesis of Changing Cold Regions Network (CCRN) research in the interior of western Canada—Part 2: Future change in cryosphere, vegetation, and hydrology. *Hydrol. Earth Syst. Sci.*, **25**, 1849–1882, https://doi.org/10.5194/hess-25-1849-2021.

Dee, D. P., and Coauthors, 2011: The ERA-Interim reanalysis: Configuration and performance of the data assimilation system. *Quart. J. Roy. Meteor. Soc.*, **137**, 553–597, https://doi.org/10.1002/qj.828.

Derksen, C., R. Brown, and M. MacKay, 2008: Mackenzie basin snow cover: Variability and trends from conventional data, satellite remote sensing, and Canadian regional climate model simulations. *Cold Region Atmospheric and Hydrologic Studies. The Mackenzie GEWEX Experience*, M. K. Woo, Eds., Springer, 213–239, https://doi.org/10.1007/978-3-540-73936-4_13.

Diaconescu, E. P., and Coauthors, 2023: An inventory of historical climate data and climate projections for the Canadian North. Government of Canada, 698 pp., https://www.canada.ca/en/environment-climate-change/services/climate-change/canadian-centre-climate-services/basics/trends-projections/historical-data-projections-canadian-north.html.

Diksha, A. Kumar, and P. Lal, 2022: Analysing climatic variability and extremes events in the Himalayan regions focusing on mountainous urban agglomerations. *Geocarto Int.*, **37**, 14 148–14 170, https://doi.org/10.1080/10106049.2022.2086635.

Dong, B., R. T. Sutton, and L. J. Wilcox, 2023: Decadal trends in surface solar radiation and cloud cover over the North Atlantic sector during the last four decades: Drivers and physical processes. *Climate Dyn.*, **60**, 2533–2546, https://doi.org/10.1007/s00382-022-06438-3.

Dörnhöfer, K., and N. Oppelt, 2016: Remote sensing for lake research and monitoring—Recent advances. *Ecol. Indic.*, **64**, 105–122, https://doi.org/10.1016/j.ecolind.2015.12.009.

Duguay, C. R., T. D. Prowse, B. R. Bonsal, R. D. Brown, M. P. Lacroix, and P. Ménard, 2006: Recent trends in Canadian lake ice cover. *Hydrol. Processes*, **20**, 781–801, https://doi.org/10.1002/hyp.6131.

ECCC, 2022: Canadian climate normal. https://climate.weather.gc.ca/climate_normals/index_e.html.

Ecosystem Classification Group, 2009: Ecological regions of the northwest territories, Taiga Plains. Department of Environment and Natural Resources, Government of the Northwest, 184 pp., https://www.gov.nt.ca/sites/ecc/files/resources/taiga_plains_ecological_land_classification_report.pdf.

Fabris, L., R. L. Rolick, B. L. Kurylyk, and S. K. Carey, 2020: Characterization of contrasting flow and thermal regimes in two adjacent subarctic alpine headwaters in northwest Canada. *Hydrol. Processes*, **34**, 3252–3270, https://doi.org/10.1002/hyp.13786.

Fink, G., M. Schmid, B. Wahl, T. Wolf, and A. Wüest, 2014: Heat flux modifications related to climate-induced warming of large European Lakes. *Water Resour. Res.*, **50**, 2072–2085, https://doi.org/10.1002/2013WR014448.

Garibaldi, M. C., P. P. Bonnaventure, S. L. Smith, and C. Duchesne, 2022: Active layer variability and change in the Mackenzie Valley, northwest territories between 1991–2014: An ecoregional assessment. *Arct. Antarct. Alp. Res.*, **54**, 274–293, https://doi.org/10.1080/15230430.2022.2097156.

GNWT, 2018: 2030 NWT climate change strategic framework. 108 pp., https://www.enr.gov.nt.ca/sites/enr/files/resources/128-climate_change_strategic_framework_web.pdf.

Green, J. K., A. G. Konings, S. H. Alemohammad, J. Berry, D. Entekhabi, J. Kolassa, J.-E. Lee, and P. Gentine, 2017: Regionally strong feedbacks between the atmosphere and terrestrial biosphere. *Nat. Geosci.*, **10**, 410–414, https://doi.org/10.1038/ngeo2957.

Hasenauer, H., K. Merganicova, R. Petritsch, S. A. Pietsch, and P. E. Thornton, 2003: Validating daily climate interpolations over complex terrain in Austria. *Agric. For. Meteor.*, **119**, 87–107, https://doi.org/10.1016/S0168-1923(03)00114-X.

Haynes, K. M., O. A. Carpino, R. F. Connon, É. Devoie, and W. L. Quinton, 2019: Thaw-induced land-cover change in the southern margin of discontinuous permafrost, northeastern British Columbia and southwestern northwest territories. 10 pp., https://ba-cdn.sfo3.digitaloceanspaces.com/Clients/Geoscience/pdf/Paper-25-Web-Final.pdf.

Heo, E.-S., M.-K. Sung, S.-I. An, and Y.-M. Yang, 2021: Decadal phase shift of summertime Arctic dipole pattern and its nonlinear effect on sea ice extent. *Int. J. Climatol.*, **41**, 4732–4742, https://doi.org/10.1002/joc.7097.

Hersbach, H., and Coauthors, 2020: The ERA5 global reanalysis. *Quart. J. Roy. Meteor. Soc.*, **146**, 1999–2049, https://doi.org/10.1002/qj.3803.

Hinkel, K. M., and Coauthors, 2012: Thermokarst lakes on the Arctic coastal plain of Alaska: Spatial and temporal variability in summer water temperature. *Permafrost Periglacial Processes*, **23**, 207–217, https://doi.org/10.1002/ppp.1743.

Hu, C., Y. Wang, W. Wang, S. Liu, M. Piao, W. Xiao, and X. Lee, 2017: Trends in evaporation of a large subtropical lake. *Theor. Appl. Climatol.*, **129**, 159–170, https://doi.org/10.1007/s00704-016-1768-z.

Huang, Y., H. Liu, K. Hinkel, B. Yu, R. Beck, and J. Wu, 2017: Analysis of thermal structure of Arctic Lakes at local and regional scales using in situ and multidate Landsat-8 data. *Water Resour. Res.*, **53**, 9642–9658, https://doi.org/10.1002/2017WR021335.

——, and Coauthors, 2019: Thicker clouds and accelerated Arctic sea ice decline: The atmosphere-sea ice interactions in spring. *Geophys. Res. Lett.*, **46**, 6980–6989, https://doi.org/10.1029/2019GL082791.

Hungerford, R. D., R. R. Nemani, S. W. Running, and J. C. Coughlan, 1989: MTCLIM: A mountain microclimate simulation model. US Department of Agriculture, Forest Service, Intermountain Research Station, Research Paper INT-414, 56 pp., https://doi.org/10.2737/INT-RP-414.

Kejna, M., J. Uscka-Kowalkowska, and P. Kejna, 2021: The influence of cloudiness and atmospheric circulation on radiation balance and its components. *Theor. Appl. Climatol.*, **144**, 823–838, https://doi.org/10.1007/s00704-021-03570-8.

Kendall, M. G., 1970: *Rank Correlation Methods*. Griffin, 202 pp.

Kheyrollah Pour, H., C. R. Duguay, A. Martynov, and L. C. Brown, 2012: Simulation of surface temperature and ice cover of large northern lakes with 1-D models: A comparison with MODIS satellite data and *in situ* measurements. *Tellus*, **64A**, 17614, https://doi.org/10.3402/tellusa.v64i0.17614.

——, ——, R. Solberg, and Ø. Rudjord, 2014a: Impact of satellite-based lake surface observations on the initial state of HIRLAM. Part I: Evaluation of remotely-sensed lake surface water temperature observations. *Tellus*, **66A**, 21534, https://doi.org/10.3402/tellusa.v66.21534.

——, L. Rontu, C. R. Duguay, K. Eerola, and E. Kourzeneva, 2014b: Impact of satellite-based lake surface observations on the initial state of HIRLAM. Part II: Analysis of lake surface temperature and ice cover. *Tellus*, **66A**, 21395, https://doi.org/10.3402/tellusa.v66.21395.

Kuhn, C., and D. Butman, 2021: Declining greenness in Arctic-boreal Lakes. *Proc. Natl. Acad. Sci. USA*, **118**, e2021219118, https://doi.org/10.1073/pnas.2021219118.

Kwong, Y. T. J., and T. Y. Gan, 1994: Northward migration of permafrost along the Mackenzie highway and climatic warming. *Climatic Change*, **26**, 399–419, https://doi.org/10.1007/BF01094404.

Levin, D., 2017: Ice roads ease isolation in Canada's North, but they're melting too soon. *New York Times*, 15 August, https://www.nytimes.com/2017/04/19/world/canada/ice-roads-ease-isolation-in-canadas-north-but-theyre-melting-too-soon.html.

Livingstone, D. M., 2003: Impact of secular climate change on the thermal structure of a large temperate central European lake. *Climatic Change*, **57**, 205–225, https://doi.org/10.1023/A:1022119503144.

Mann, H. B., 1945: Nonparametric tests against trend. *Econometrica*, **13**, 245–259, https://doi.org/10.2307/1907187.

Mekis, E., N. Donaldson, J. Reid, A. Zucconi, J. Hoover, Q. Li, R. Nitu, and S. Melo, 2018: An overview of surface-based precipitation observations at environment and climate change Canada. *Atmos.–Ocean*, **56**, 71–95, https://doi.org/10.1080/07055900.2018.1433627.

Messager, M. L., B. Lehner, G. Grill, I. Nedeva, and O. Schmitt, 2016: Estimating the volume and age of water stored in global lakes using a geo-statistical approach. *Nat. Commun.*, **7**, 13603, https://doi.org/10.1038/ncomms13603.

Milewska, E. J., 2004: Baseline cloudiness trends in Canada 1953–2002. *Atmos.–Ocean*, **42**, 267–280, https://doi.org/10.3137/ao.420404.

Molot, L. A., J. J. Hudson, P. J. Dillon, and S. A. Miller, 2005: Effect of PH on photo-oxidation of dissolved organic carbon by hydroxyl radicals in a coloured, softwater stream. *Aquat. Sci.*, **67**, 189–195, https://doi.org/10.1007/s00027-005-0754-9.

Moslemi-Aqdam, M., and Coauthors, 2022: Understanding among-lake variability of mercury concentrations in northern Pike (*Esox lucius*): A whole-ecosystem study in subarctic lakes. *Sci. Total Environ.*, **822**, 153430, https://doi.org/10.1016/j.scitotenv.2022.153430.

Murfitt, J., and L. C. Brown, 2017: Lake ice and temperature trends for Ontario and Manitoba: 2001 to 2014. *Hydrol. Processes*, **31**, 3596–3609, https://doi.org/10.1002/hyp.11295.

NASA, 1999: Clouds & radiation fact sheet. NASA Earth Observatory, Accessed 2 September 2022, https://earthobservatory.nasa.gov/features/Clouds.

O'Reilly, C. M., and Coauthors, 2015: Rapid and highly variable warming of lake surface waters around the globe. *Geophys. Res. Lett.*, **42**, 10 773–10 781, https://doi.org/10.1002/2015GL066235.

Oswald, C. J., and W. R. Rouse, 2004: Thermal characteristics and energy balance of various-size Canadian Shield Lakes in the Mackenzie River basin. *J. Hydrometeor.*, **5**, 129–144, https://doi.org/10.1175/1525-7541(2004)005<0129:TCAEBO>2.0.CO;2.

Pareeth, S., N. Salmaso, R. Adrian, and M. Neteler, 2016: Homogenised daily lake surface water temperature data generated from multiple satellite sensors: A long-term case study of a large sub-Alpine lake. *Sci. Rep.*, **6**, 31251, https://doi.org/10.1038/srep31251.

Phillips, D. W., 1990: *The Climates of Canada.* Minister of Supply and Services Canada, 176 pp.

Pienitz, R., J. P. Smol, and D. R. S. Lean, 1997: Physical and chemical limnology of 24 lakes located between Yellowknife and Contwoyto Lake, Northwest Territories (Canada). *Can. J. Fish. Aquat. Sci.*, **54**, 347–358, https://doi.org/10.1139/f96-275.

Pilla, R. M., and R. Couture, 2021: Attenuation of photosynthetically active radiation and ultraviolet radiation in response to changing dissolved organic carbon in browning lakes: Modeling and parametrization. *Limnol. Oceanogr.*, **66**, 2278–2289, https://doi.org/10.1002/lno.11753.

Prowse, T. D., C. Furgal, B. R. Bonsal, and D. L. Peters, 2009: Climate impacts on northern Canada: Regional background. *Ambio: J. Human Environ.*, **38**, 248–256, https://doi.org/10.1579/0044-7447-38.5.248.

Przybylak, R., P. N. Svyashchennikov, J. Uscka-Kowalkowska, and P. Wyszyński, 2021: Solar radiation in the Arctic during the early twentieth-century warming (1921–50): Presenting a compilation of newly available data. *J. Climate*, **34**, 21–37, https://doi.org/10.1175/JCLI-D-20-0257.1.

Råman Vinnå, L., I. Medhaug, M. Schmid, and D. Bouffard, 2021: The vulnerability of lakes to climate change along an altitudinal gradient. *Commun. Earth Environ.*, **2**, 35, https://doi.org/10.1038/s43247-021-00106-w.

Rouse, W. R., and Coauthors, 1997: Effects of climate change on the freshwaters of Arctic and subarctic North America. *Hydrol. Processes*, **11**, 873–902, https://doi.org/10.1002/(SICI)1099-1085(19970630)11:8<873::AID-HYP510>3.0.CO;2-6.

——, C. J. Oswald, J. Binyamin, C. Spence, W. M. Schertzer, P. D. Blanken, N. Bussières, and C. R. Duguay, 2005: The role of northern lakes in a regional energy balance. *J. Hydrometeor.*, **6**, 291–305, https://doi.org/10.1175/JHM421.1.

Sanchez-Lorenzo, A., M. Wild, M. Brunetti, J. A. Guijarro, M. Z. Hakuba, J. Calbó, S. Mystakidis, and B. Bartok, 2015: Reassessment and update of long-term trends in downward surface shortwave radiation over Europe (1939–2012). *J. Geophys. Res. Atmos.*, **120**, 9555–9569, https://doi.org/10.1002/2015JD023321.

Schaeffer, B. A., J. Iiames, J. Dwyer, E. Urquhart, W. Salls, J. Rover, and B. Seegers, 2018: An initial validation of Landsat 5 and 7 derived surface water temperature for U.S. lakes, reservoirs, and estuaries. *Int. J. Remote Sens.*, **39**, 7789–7805, https://doi.org/10.1080/01431161.2018.1471545.

Schindler, D. W., P. J. Curtis, S. E. Bayley, B. R. Parker, K. G. Beaty, and M. P. Stainton, 1997: Climate-induced changes in the dissolved organic carbon budgets of boreal lakes. *Biogeochemistry*, **36**, 9–28, https://doi.org/10.1023/A:1005792014547.

Schmid, M., and O. Köster, 2016: Excess warming of a central European lake driven by solar brightening. *Water Resour. Res.*, **52**, 8103–8116, https://doi.org/10.1002/2016WR018651.

——, and J. Read, 2022: Heat budget of lakes. *Encyclopedia of Inland Waters*, 2nd ed. T. Mehner and K. Tockner, Eds., Elsevier, 467–473, https://doi.org/10.1016/B978-0-12-819166-8.00011-6.

Serreze, M. C., and R. G. Barry, 2014: *The Arctic Climate System.* 2nd ed. Cambridge University Press, 404 pp.

Sharaf, N., A. Fadel, M. Bresciani, C. Giardino, B. J. Lemaire, K. Slim, G. Faour, and B. Vinçon-Leite, 2019: Lake surface temperature retrieval from Landsat-8 and retrospective analysis in Karaoun Reservoir, Lebanon. *J. Appl. Remote Sens.*, **13**, 044505, https://doi.org/10.1117/1.JRS.13.044505.

Sharma, S., D. A. Jackson, C. K. Minns, and B. J. Shuter, 2007: Will northern fish populations be in hot water because of climate change? *Global Change Biol.*, **13**, 2052–2064, https://doi.org/10.1111/j.1365-2486.2007.01426.x.

Shook, K., and J. Pomeroy, 2011: Synthesis of incoming shortwave radiation for hydrological simulation. *Hydrol. Res.*, **42**, 433–446, https://doi.org/10.2166/nh.2011.074.

Stettz, S., B. F. Zaitchik, D. Ademe, S. Musie, and B. Simane, 2019: Estimating variability in downwelling surface shortwave radiation in a tropical highland environment. *PLOS ONE*, **14**, e0211220, https://doi.org/10.1371/journal.pone.0211220.

Thompson, H. D., S. J. Déry, P. L. Jackson, and B. E. Laval, 2020: A synoptic climatology of potential seiche-inducing winds in a large intermontane lake: Quesnel Lake, British Columbia, Canada. *Int. J. Climatol.*, **40**, 5973–5986, https://doi.org/10.1002/joc.6560.

Thornton, P. E., and S. W. Running, 1999: An improved algorithm for estimating incident daily solar radiation from measurements of temperature, humidity, and precipitation. *Agric. For. Meteor.*, **93**, 211–228, https://doi.org/10.1016/S0168-1923(98)00126-9.

——, ——, and M. A. White, 1997: Generating surfaces of daily meteorological variables over large regions of complex terrain.

J. Hydrol., **190**, 214–251, https://doi.org/10.1016/S0022-1694(96)03128-9.

——, H. Hasenauer, and M. A. White, 2000: Simultaneous estimation of daily solar radiation and humidity from observed temperature and precipitation: An application over complex terrain in Austria. *Agric. For. Meteor.*, **104**, 255–271, https://doi.org/10.1016/S0168-1923(00)00170-2.

——, R. Shrestha, M. Thornton, S.-C. Kao, Y. Wei, and B. E. Wilson, 2021: Gridded daily weather data for North America with comprehensive uncertainty quantification. *Sci. Data*, **8**, 190, https://doi.org/10.1038/s41597-021-00973-0.

Tian, D., G. Xie, J. Tian, K.-H. Tseng, C. K. Shum, J. Lee, and S. Liang, 2017: Spatiotemporal variability and environmental factors of Harmful Algal Blooms (HABs) over western Lake Erie. *PLOS ONE*, **12**, e0179622, https://doi.org/10.1371/journal.pone.0179622.

Twomey, S., 1976: Computations of the absorption of solar radiation by clouds. *J. Atmos. Sci.*, **33**, 1087–1091, https://doi.org/10.1175/1520-0469(1976)033<1087:COTAOS>2.0.CO;2.

van de Poll, W. H., D. S. Maat, P. Fischer, R. J. W. Visser, C. P. D. Brussaard, and A. G. J. Buma, 2021: Solar radiation and solar radiation driven cycles in warming and freshwater discharge control seasonal and inter-annual phytoplankton chlorophyll *a* and taxonomic composition in a high Arctic fjord (Kongsfjorden, Spitsbergen). *Limnol. Oceanogr.*, **66**, 1221–1236, https://doi.org/10.1002/lno.11677.

Vanhellemont, Q., 2020: Automated water surface temperature retrieval from Landsat 8/TIRS. *Remote Sens. Environ.*, **237**, 111518, https://doi.org/10.1016/j.rse.2019.111518.

Vincent, L. A., and É. Mekis, 2006: Changes in daily and extreme temperature and precipitation indices for Canada over the twentieth century. *Atmos.–Oceans*, **44**, 177–193, https://doi.org/10.3137/ao.440205.

Wang, K., D. Wu, K. Wu, K. Yu, and C. Zheng, 2023: Interdecadal variation trend of Arctic wind energy. *Energies*, **16**, 6545, https://doi.org/10.3390/en16186545.

Weston, S. T., W. G. Bailey, L. J. B. McArthur, and O. Hertzman, 2007: Interannual solar and net radiation trends in the Canadian Arctic. *J. Geophys. Res.*, **112**, D10105, https://doi.org/10.1029/2006JD008000.

Wielicki, B. A., B. R. Barkstrom, E. F. Harrison, R. B. Lee III, G. L. Smith, and J. E. Cooper, 1996: Clouds and the Earth's Radiant Energy System (CERES): An Earth observing system experiment. *Bull. Amer. Meteor. Soc.*, **77**, 853–868, https://doi.org/10.1175/1520-0477(1996)077<0853:CATERE>2.0.CO;2.

Wild, M., 2009: Global dimming and brightening: A review. *J. Geophys. Res.*, **114**, D00D16, https://doi.org/10.1029/2008JD011470.

——, and B. Liepert, 2010: The Earth radiation balance as driver of the global hydrological cycle. *Environ. Res. Lett.*, **5**, 025203, https://doi.org/10.1088/1748-9326/5/2/025203.

Wilks, D. S., 2006: *Statistical Methods in the Atmospheric Sciences.* 2nd ed. Academic Press, 627 pp.

Wloczyk, C., R. Richter, E. Borg, and W. Neubert, 2006: Sea and lake surface temperature retrieval from Landsat thermal data in northern Germany. *Int. J. Remote Sens.*, **27**, 2489–2502, https://doi.org/10.1080/01431160500300206.

Woolway, R. I., and C. J. Merchant, 2017: Amplified surface temperature response of cold, deep lakes to inter-annual air temperature variability. *Sci. Rep.*, **7**, 4130, https://doi.org/10.1038/s41598-017-04058-0.

——, E. Jennings, T. Shatwell, M. Golub, D. C. Pierson, and S. C. Maberly, 2021: Lake heatwaves under climate change. *Nature*, **589**, 402–407, https://doi.org/10.1038/s41586-020-03119-1.

——, S. Sharma, and J. P. Smol, 2022: Lakes in hot water: The impacts of a changing climate on aquatic ecosystems. *BioScience*, **72**, 1050–1061, https://doi.org/10.1093/biosci/biac052.

Yuan, M., T. Leirvik, and M. Wild, 2021: Global trends in downward surface solar radiation from spatial interpolated ground observations during 1961–2019. *J. Climate*, **34**, 9501–9521, https://doi.org/10.1175/JCLI-D-21-0165.1.

Yue, S., P. Pilon, B. Phinney, and G. Cavadias, 2002: The influence of autocorrelation on the ability to detect trend in hydrological series. *Hydrol. Processes*, **16**, 1807–1829, https://doi.org/10.1002/hyp.1095.

Zhang, T., K. Stamnes, and S. A. Bowling, 1996: Impact of clouds on surface radiative fluxes and snowmelt in the Arctic and subarctic. *J. Climate*, **9**, 2110–2123, https://doi.org/10.1175/1520-0442(1996)009<2110:IOCOSR>2.0.CO;2.

Zhang, X., L. A. Vincent, W. D. Hogg, and A. Niitsoo, 2000: Temperature and precipitation trends in Canada during the 20th century. *Atmos.–Ocean*, **38**, 395–429, https://doi.org/10.1080/07055900.2000.9649654.

Zhang, Y., J. Shen, L. He, J. Feng, L. Chi, and X. Wang, 2024: Challenge to lake ecosystems: Changes in thermal structure triggered by climate change. *Water*, **16**, 888, https://doi.org/10.3390/w16060888.